

April 2, 2021

# A Simple Explicit-Solvent Model of Polyampholyte Phase Behaviors and its Ramifications for Dielectric Effects in Biomolecular Condensates

Jonas WESSÉN,<sup>1,†</sup> Tanmoy PAL,<sup>1,†</sup> Suman DAS,<sup>1,†</sup> Yi-Hsuan LIN,<sup>1,2</sup> and  
Hue Sun CHAN<sup>1,\*</sup>

<sup>1</sup>Department of Biochemistry, University of Toronto, Toronto, Ontario M5S 1A8, Canada;

<sup>2</sup>Molecular Medicine, Hospital for Sick Children, Toronto, Ontario M5G 0A4, Canada

† Contributed equally to this work.

\*Corresponding author

E-mail: chan@arrhenius.med.utoronto.ca; Tel: (416)978-2697; Fax: (416)978-8548

Mailing address:

Department of Biochemistry, University of Toronto, Medical Sciences Building – 5th Fl.,  
1 King's College Circle, Toronto, Ontario M5S 1A8, Canada.

## Abstract

Biomolecular condensates such as membraneless organelles, underpinned by liquid-liquid phase separation (LLPS), are important for physiological function, with electrostatics—among other interaction types—being a prominent force in their assembly. Charge interactions of intrinsically disordered proteins (IDPs) and other biomolecules are sensitive to the aqueous dielectric environment. Because the relative permittivity of protein is significantly lower than that of water, the interior of an IDP condensate is a relatively low-dielectric regime, which, aside from its possible functional effects on client molecules, should facilitate stronger electrostatic interactions among the scaffold IDPs. To gain insight into this LLPS-induced dielectric heterogeneity, addressing in particular whether a low-dielectric condensed phase entails more favorable LLPS than that posited by assuming IDP electrostatic interactions are uniformly modulated by the higher dielectric constant of the pure solvent, we consider a simplified multiple-chain model of polyampholytes immersed in explicit solvents that are either polarizable or possess a permanent dipole. Notably, simulated phase behaviors of these systems exhibit only minor to moderate differences from those obtained using implicit-solvent models with a uniform relative permittivity equals to that of pure solvent. Buttressed by theoretical treatments developed here using random phase approximation and polymer field-theoretic simulations, these observations indicate a partial compensation of effects between favorable solvent-mediated interactions among the polyampholytes in the condensed phase and favorable polyampholyte-solvent interactions in the dilute phase, often netting only a minor enhancement of overall LLPS propensity from the very dielectric heterogeneity that arises from the LLPS itself. Further ramifications of this principle are discussed.

## INTRODUCTION

Biomolecular condensates,<sup>1</sup>—physico-chemically based in large measure upon liquid-liquid phase separation (LLPS)<sup>2–5</sup> underpinned by multivalent interactions among intrinsically disordered proteins (IDPs), proteins containing intrinsically disordered regions (IDRs), folded domains, folded proteins, and nucleic acids<sup>6–11</sup>—are now widely recognized as a means for living organisms, eukaryotes as well as prokaryotes, to functionally compartmentalize their internal space.<sup>12–15</sup> Among their multifaceted physiological roles,<sup>1,16–19</sup> the droplet-like condensates, especially the intracellular varieties referred to as membraneless organelles, provide specialized, tunable micro-environments, distinct from their surroundings, that facilitate certain biochemical processes.<sup>20,21</sup> One of the many possible mechanisms by which they serve this task is by preferential partitioning of certain reactants into the condensates. Examples include retention of selected types of small nuclear ribonucleoproteins in Cajal bodies, a function likely plays a critical role in pre-mRNA splicing,<sup>22</sup> partitioning of single-stranded but not double-stranded DNA into condensates of RNA helicase Ddx4 that mimic nuage membraneless organelles—thus serving probably as a molecular filter for functional nucleic acid processing,<sup>9,23</sup> and concentration of transcription regulators in TAZ (tafazzin) nuclear condensates to promote gene expression.<sup>24</sup>

LLPS of IDPs/IDRs is known to underlie an increasing number of biomolecular condensates,<sup>25</sup> as exemplified by well-studied condensates of N-terminal IDR domains of, respectively, the DEAD-box RNA helicase 4 (Ddx4),<sup>9</sup> the RNA-binding protein fused in sacroma (FUS),<sup>26</sup> and the P-granule DEAD-box RNA helicase LAF-1.<sup>27</sup> Compared to amino acid sequences encoding for globular proteins, IDPs/IDRs are depleted of hydrophobic but enriched with polar and charged residues.<sup>28</sup> Consistent with these trends, electrostatics is one of the major driving forces for biomolecular LLPS,<sup>4,9,29,30</sup> together with cation- $\pi$  and  $\pi$ - $\pi$  interactions which can be equally or sometimes even more important,<sup>31–35</sup> and hydrophobic interactions which can be important<sup>36</sup> for systems that exhibit a lower critical solution temperature<sup>37–39</sup> rather than an upper critical solution temperature.<sup>40</sup> As far as electrostatics is concerned,<sup>41,42</sup> experiments on a charge scrambled mutant of Ddx4,<sup>9</sup> phosphorylated variants of FUS,<sup>26</sup> phosphorylated variants of an IDR of the fragile X mental retardation protein (FMRP),<sup>43</sup> and charge shuffled variants of LAF-1<sup>44</sup> indicate that effects of charged interactions on LLPS and complexation behaviors depend not only on an IDP/IDR's net charge but also its sequence charge pattern.<sup>4,45–50</sup> Recently, some of these and related sequence-dependent effects on LLPS have been modeled successfully and rationalized by polymer theory using random phase approximation (RPA),<sup>4,29,51</sup> restricted primitive models,<sup>52</sup> Kuhn length renormalization,<sup>53</sup> coarse-grained explicit-chain molecular dynamics (MD)<sup>35,44,54–58</sup> and Monte Carlo<sup>59</sup> sampling, and field-theoretic simulations.<sup>60–64</sup>

In these recent theoretical and computational studies of electrostatic effects in LLPS, the relative permittivity,  $\epsilon_r$ , for the solvent-mediated intra- and interchain electrostatic interactions among charged IDPs are often taken to be uniform and equal to that of bulk water ( $\epsilon_r \approx 80$ ),<sup>39,44,52,54–56,58,60</sup> or left unspecified as a constant  $\epsilon_r$  that is subsumed in the Bjerrum length or a reduced temperature,<sup>29,48,51,53,57,61–63</sup> or as a fitting parameter for matching theory to experiment, yielding constant  $\epsilon_r$  values in the range of  $\approx 30$ – $60$ , which are smaller than but still within the same order of magnitude of that of bulk water.<sup>4,9,29</sup> A common feature of these formulations is that while the value of  $\epsilon_r$  may differ from model to model,  $\epsilon_r$  is always assumed to be a position-independent constant for a given model irrespective of the local IDP density. However, proteins<sup>65–71</sup> and nucleic acids<sup>72</sup> have substantially lower relative permittivities than bulk water. Inside the droplet, the density of water is reduced because of the higher concentrations of protein and nucleic acids. Moreover, the water molecules that remain, being likely near protein surfaces, generally entail a smaller relative permittivity than that of bulk water due to restrictions on their rotational freedom.<sup>73</sup> Taken together, these considerations lead one to expect that the effective permittivity<sup>51,74–77</sup> inside a condensed-phase IDP droplet is lower than that of the dilute phase.<sup>78</sup> Such a different dielectric environment could affect the behaviors of proteins and nucleic acids<sup>79,80</sup> as well as the partitioning and sequestration of a variety of “client” molecules in the condensed droplet<sup>81</sup> and thus contribute to the maintenance of biomolecular condensates and the functional biophysical and biochemical processes within them.<sup>82–85</sup>

The significantly different dielectric environments expected for the dilute phase on one hand and the condensed phase on the other raise basic questions regarding the aforementioned common practice of using a single, constant  $\epsilon_r$ —rather than a variable  $\epsilon_r$  that depends on local IDP density—for the electrostatic interactions in LLPS theories and computational models. One obvious concern is that because the effective  $\epsilon_r$  inside the condensed phase is substantially lower than that of water, the LLPS-driving electrostatic interactions in the condensed phase should be modulated by this lower value of  $\epsilon_r$  and therefore much stronger than that posited by assuming a uniform  $\epsilon_r$  of bulk water. This consideration suggests that the propensity to phase separate can be much higher than that predicted by assuming a constant  $\epsilon_r$ . In apparent agreement with this intuition, earlier studies using modified RPA formulations with an  $\epsilon_r(\phi)$  that depends on IDP volume fraction  $\phi$  show significant increases in LLPS propensities.<sup>29,51</sup> Subsequently, however, a more nuanced analysis that takes into account a “self-energy” term in the  $\epsilon_r \rightarrow \epsilon_r(\phi)$  RPA formulation indicates that there is a trade-off between the enhanced effective electrostatic interactions among the IDPs in the condensed phase (which tend to increase LLPS propensity) and the enhanced interactions between the IDPs and the solvent in the dilute phase (which tend to decrease LLPS propensity), resulting in a relative minor overall effect on LLPS propensity.<sup>35</sup>

While the insights provided by these preliminary investigations are valuable—not the

least for formulating the questions needed to be tackled, our understanding of the effect of the biomolecule-dependent dielectric environment on the energetics of LLPS remains quite limited. This is because the  $\epsilon_r(\phi)$  in these formulations are obtained from effective medium theories<sup>74–76</sup> based on an implicit treatment of water rather than having dielectric properties emerge from an explicit model of water. Indeed, a shortcoming of this approach is that predictions based on different effective medium theories can differ substantially.<sup>29,35,51</sup> With this in mind, the present work aims to attain a more definitive physical picture by modeling sequence-dependent LLPS of polyampholytes with an explicit polar solvent. Recently, new insights have been gained into the interactions between salt ions and protein as well as the diffusive dynamics in condensed FUS and LAF-1 IDR droplets by using the TIP4P/2005 model of water.<sup>86</sup> The explicit water model, however, is absent in the initial thermodynamic simulation to assemble the condensed phase. Separately, explicit coarse-grained water has been applied successfully to simulate condensates of FUS IDR<sup>87</sup> using the MARTINI coarse-grained force field,<sup>88</sup> though polar versions of the coarse-grained water model<sup>89</sup> is not employed. Since our goal is to better understand the general physical principles rather than to achieve quantitative match with experiment, here we take a complementary approach by using simple dipoles—each consisting only of one positive and one negative charge—as a model for a water-like polar solvent. In this regard, our construct shares similarities with a simple lattice dipole model of water restricted to an essentially one-dimensional configuration<sup>90</sup> as well as three-dimensional simple dipole models for polar liquids.<sup>91</sup> Unlike our previous implicit-solvent formulations,<sup>29,35,51</sup> here the different dielectric environments for the dilute and condensed phases arise physically from the polar nature of the dipoles rather than as a prescribed function of local solvent and IDP concentrations alone. Importantly, the model’s simplicity allows equilibrated LLPS systems comprising of both explicit dipole solvent molecules and polyampholytes to be simulated.

Consistent with the trend observed in a recent implicit-solvent RPA analysis that include a self-energy term,<sup>35</sup> polyampholyte phase properties simulated in explicit-chain models with the present explicit dipole model of polar solvent are quantitatively similar to—albeit not identical with—those simulated without the explicit solvent but with a uniform relative permittivity corresponding to that of the pure polar solvent. Whether the LLPS propensity of the explicit-solvent system is slightly higher or slightly lower than that of the corresponding implicit-solvent system likely depends on the system’s structural and energetic details. Nonetheless, our results suggest, assuringly, that the error in employing an IDP-concentration-independent bulk-water  $\epsilon_r \approx 80$  in LLPS simulations<sup>39,44,52,54–56,58,60</sup> may be relatively small even when the dielectric environments inside and outside of the condensed phase are significantly different. To address the generality of this putative principle, we have also developed corresponding field-theory formulations for polyampholytes with a polar solvent modeled as permanent or polarizable dipoles that are treated

explicitly in the theory. Similar permanent<sup>92–94</sup> and polarizable<sup>95,96</sup> dipole models were used to study dielectric properties of polar solutions<sup>92–96</sup> and the effect of electric field on phase stability of charged polymers;<sup>97</sup> but have not been applied to tackle the question at hand. Here we find that the trend of phase behaviors predicted using RPA of our field-theory formulation regarding explicit versus implicit solvent are in agreement with that obtained by explicit-chain simulations, suggesting that a compensation between more favorable polyampholyte-polar-solvent electrostatic interactions in a high- $\epsilon_r$  dilute phase and more favorable effective inter-polyampholyte electrostatic interactions in a low- $\epsilon_r$  condensed phase is a rather robust feature of polyampholyte LLPS systems. Details of our methodology and findings are described below.

## MODELS AND METHODS

The formulation and computational methodology of our coarse-grained explicit-chain model of polyampholyte LLPS in the presence of explicit dipoles as a model polar solvent is adapted from—and follows largely—a protocol developed recently for implicit-solvent simulations of LLPS of chain molecules,<sup>54,56,98</sup> an approach our group has applied previously to study LLPS of model polyampholytes<sup>57</sup> and to address experimental data on IDR LLPS.<sup>35</sup> Following refs. 55, 57, but with a notation more in line with that in ref. 53, let  $n_p$  be the total number of polyampholyte chains in the system which are labeled by  $\mu, \nu = 1, 2, \dots, n_p$ , let  $N$  be the number of monomers (beads) in each chain, labeled by  $i, j = 1, 2, \dots, N$ , and  $n_w$  be the total number of dipoles (which may be viewed as serving as model water molecules and hence the subscript “w”) which are labeled by  $v = 1, 2, \dots, n_w$ . Note that a dipole in the present formulation is equivalent to a polyampholytic dimer chain carrying a pair of opposite charges, denoted here as  $q_d = \pm|q_d|$ , on its two monomer beads.

The total potential energy  $U_T$ , expressed in the equation below as a sum of contributions, is a function of the positions of the monomers in the polyampholyte chains and in the dipoles:

$$U_T = U_{\text{bond}} + U_{\text{LJ}} + U_{\text{el}} \quad (1)$$

with  $U_{\text{bond}}$  being the bond-length term for chain connectivity that applies to the polyampholytes as well as the dipoles:

$$U_{\text{bond}} = \frac{K_{\text{bond}}}{2} \left[ \sum_{\mu=1}^{n_p} \sum_{i=1}^{N-1} (r_{\mu i, \mu i+1} - a)^2 + \sum_{v=1}^{n_w} (r_{v+, v-} - a)^2 \right] \quad (2)$$

where, in general,  $r_{\mu i, \nu j}$  is the distance between monomer  $i$  in polyampholyte chain  $\mu$  and monomer  $j$  in polyampholyte chain  $\nu$ ,  $r_{v\pm, v'\pm}$  is the distance between the position of the positive (+) or negative (−) charge on dipole  $v$  and the position of the positive (+) or

negative ( $-$ ) charge on dipole  $v'$ , and  $a$  is the reference bead-bead bond length that serves as the length scale of the model. Here we set  $K_{\text{bond}} = 75,000\varepsilon/a^2$ , where  $\varepsilon$  is an energy scale to be defined below. This value of  $K_{\text{bond}}$ , which is in line with the TraPPE force field,<sup>99–102</sup> entails a very stiff spring constant;<sup>50,57,98</sup> thus the dipoles are essentially permanent (fixed) dipoles (with magnitude of dipole moment  $\mu \approx |q_d|a$ ) because they are practically not polarizable by fluctuation of the bond length ( $\approx a$ ) between a dipole's  $\pm|q_d|$  beads.  $q_d$  is given in units of the elementary protonic charge,  $e$ , below. (The symbol  $\mu$  for dipole moment magnitude is not to be confused with the polyampholyte label  $\mu = 1, 2, \dots, n_p$ ).

$U_{\text{LJ}}$  in the above Eq. 1 accounts for the non-bonded Lennard-Jones-like interactions, which in the present model takes different forms depending on whether the monomer beads involved are both from polyampholyte chains (pp), both from dipoles (dd), or one from a polyampholyte chain and the other from a dipole (pd):

$$U_{\text{LJ}} = U_{\text{LJ,pp}} + U_{\text{LJ,dd}} + U_{\text{LJ,pd}}. \quad (3)$$

As before,<sup>57</sup> the polyampholyte-polyampholyte term  $U_{\text{LJ,pp}}$  is the standard 12-6 LJ potential:

$$U_{\text{LJ,pp}} = 4\varepsilon_{\text{LJ}} \sum_{\substack{\mu, \nu=1 \\ (\mu, i) \neq (\nu, j)}}^{n_p} \sum_{i, j=1}^N \left[ \left( \frac{a}{r_{\mu i, \nu j}} \right)^{12} - \left( \frac{a}{r_{\mu i, \nu j}} \right)^6 \right], \quad (4)$$

where  $\varepsilon_{\text{LJ}}$  is the well depth and the bead diameter  $a$  is equal to the reference bond length in Eq. 2. During simulation,  $U_{\text{LJ,pp}}$  is truncated at  $r_{\mu i, \nu j} = 6a$  for computational efficiency (individual terms in  $U_{\text{LJ,pp}}$  are set to zero for  $r_{\mu i, \nu j} \geq 6a$ ). To avoid freezing of the dipole solvent at relatively low temperatures and other complications as well as to facilitate comparison with analytical theory, the dipole-dipole and polyampholyte-dipole contributions in Eq. 3 are chosen to be consisting of only excluded-volume (ex) repulsion terms, viz.,

$$U_{\text{LJ,dd}} = \sum_{v=1}^{n_w-1} \sum_{v'=v+1}^{n_w} [\tilde{U}_{\text{LJ}}^{\text{ex}}(r_{v+, v'+}) + \tilde{U}_{\text{LJ}}^{\text{ex}}(r_{v-, v'-}) + \tilde{U}_{\text{LJ}}^{\text{ex}}(r_{v+, v'-}) + \tilde{U}_{\text{LJ}}^{\text{ex}}(r_{v-, v'+})] \quad (5)$$

and

$$U_{\text{LJ,pd}} = \sum_{\mu=1}^{n_p} \sum_{i=1}^N \sum_{v=1}^{n_w} [\tilde{U}_{\text{LJ}}^{\text{ex}}(r_{\mu i, v+}) + \tilde{U}_{\text{LJ}}^{\text{ex}}(r_{\mu i, v-})], \quad (6)$$

where the individual purely repulsive terms in the above summations take the Weeks-Chandler-Andersen form:<sup>103</sup>

$$\tilde{U}_{\text{LJ}}^{\text{ex}}(r) \equiv \begin{cases} \tilde{U}_{\text{LJ}}(r) + \varepsilon_{\text{LJ}}, & \text{for } r \leq 2^{1/6}a \\ 0, & \text{for } r > 2^{1/6}a \end{cases} \quad (7)$$

which is obtained, as specified here, by performing a cutoff and a shift on an individual standard LJ term  $\tilde{U}_{\text{LJ}}(r) \equiv 4\epsilon_{\text{LJ}}[(a/r)^{12} - (a/r)^6]$  in Eq. 4.

Similar to Eq. 3, the electrostatic interaction  $U_{\text{el}}$  in Eq. 1 is written as a sum of pp, dd, and pd components:

$$U_{\text{el}} = U_{\text{el,pp}} + U_{\text{el,dd}} + U_{\text{el,pd}}. \quad (8)$$

The polyampholyte-polyampholyte contribution is given by

$$U_{\text{el,pp}} = \sum_{\substack{\mu,\nu=1 \\ (\mu,i) \neq (\nu,j)}}^{n_p} \sum_{i,j=1}^N \frac{\sigma_i \sigma_j e^2}{4\pi\epsilon_0\epsilon_r r_{\mu i, \nu j}}, \quad (9)$$

where  $\sigma_i$  is the charge of the  $i$ th monomer bead in units of elementary protonic charge  $e$ , ( $\sigma_i$  depends on the polyampholyte sequence but is independent of  $\mu, \nu$ ), and  $\epsilon_0$  is vacuum permittivity. For simulation with explicit dipoles, relative permittivity  $\epsilon_r$  is set to unity for the  $U_{\text{el,pp}}$  term in Eq. 9; but  $\epsilon_r > 1$  can be included in implicit-solvent simulations. The other contributions in Eq. 8 which involve the dipoles are given by:

$$U_{\text{el,dd}} = \sum_{v=1}^{n_w-1} \sum_{v'=v+1}^{n_w} \frac{q_d^2 e^2}{4\pi\epsilon_0} \left( \frac{1}{r_{v+,v'+}} + \frac{1}{r_{v-,v'-}} - \frac{1}{r_{v+,v'-}} - \frac{1}{r_{v-,v'+}} \right), \quad (10)$$

where the charges  $q_d$  on the dipoles are in units of elementary protonic charge  $e$ , and

$$U_{\text{el,pd}} = \sum_{\mu=1}^{n_p} \sum_{i=1}^N \sum_{v=1}^{n_w} \frac{\sigma_i q_d e^2}{4\pi\epsilon_0} \left( \frac{1}{r_{\mu i, v+}} - \frac{1}{r_{\mu i, v-}} \right). \quad (11)$$

As in ref. 57, the energy scale  $\epsilon$  introduced above in conjunction with  $K_{\text{bond}}$  is chosen to be the strength of electrostatic interactions at a monomer-monomer separation  $a$  for the polyampholytes, i.e.,  $\epsilon = e^2/(4\pi\epsilon_0\epsilon_r a)$ , and the well depth  $\epsilon_{\text{LJ}}$  of LJ-like interactions in Eq. 4 is set to be equal to  $\epsilon$ , i.e.,  $\epsilon_{\text{LJ}} = \epsilon$ , as in Fig. 4a of ref. 57. These specifications complete the description of the total potential energy function  $U_{\text{T}}$  in Eq. 1 used in our simulations.

Fig. 1 depicts the  $N = 50$  model polyampholyte sequences and the model dipole solvent molecule used in this study. The three overall neutral sequences (each containing 25 positive and 25 negative beads), sv15, sv20, and sv30, were introduced by Das and Pappu.<sup>45</sup> These sequences have been used in recent explicit-chain simulations of sequence-dependent IDP binding and LLPS.<sup>50,57</sup> Here, they serve to assess whether the sequence-dependent LLPS observed in explicit-chain, implicit-solvent simulations<sup>57,58</sup> holds for explicit-chain-simulated LLPS in the presence of explicit dipole solvent molecules, bearing in mind that these sequences cover a considerable variation of charge patterns as quantitatively characterized by the intuitive blockiness parameter  $\kappa$  (ref. 45;  $\kappa = 0.1354, 0.2721, \text{ and } 1.0$ , respectively,

for sv15, sv20, and sv30) and the theory-derived “sequence charge decoration” parameter<sup>46</sup> (SCD;  $-SCD = 4.35, 7.37, \text{ and } 27.8$ , respectively, for sv15, sv20, and sv30).

Regarding sv sequences, it should be noted that  $U_{LJ,pp}$  in Eq. 4, which contains an attractive interaction, is used here to facilitate comparison with previous explicit-chain simulation results of sv sequences employing the same potential.<sup>57</sup> While the pure repulsive  $\tilde{U}_{LJ}^{\text{ex}}$  in Eq. 7 without nonelectrostatic attraction for polyampholyte-polyampholyte interaction may appear more in line with the analytical theory to be developed below, we found that as a pure polymer system, sv15 fails to phase separate under  $\tilde{U}_{LJ}^{\text{ex}}$  (ref. 57). Effects of other LJ-type potentials with a nonzero but weakened attraction such as the “with 1/3 LJ” model in ref. 57 are worthy of further exploration but are beyond the scope of our present effort.

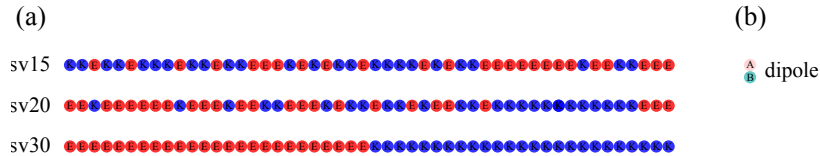


**Fig. 1:** Model polyampholytes and dipole solvent molecules. (a) The  $N = 50$  model sequences studied in the present work. As in ref. 45, positively and negatively charged monomer beads are labeled as “K” (lysine) and “E” (glutamic acid), respectively, and depicted in blue and red. (b) Dipole as model polar solvent molecule. Underscoring that the charges on the solvent dipoles can be different from those on the model polyampholytes in (a), i.e.,  $|q_d|$  does not necessarily equal unity, the positively charged (“B”, cyan) and negatively charged (“A”, pink) beads in (b) do not share the K/E and blue/red labels in (a).

As in our previous studies,<sup>35,57</sup> molecular dynamics simulations of the present model are performed by the GPU-version of the HOOMD-blue simulation package<sup>104,105</sup> using a recently developed methodology for simulating phase behaviors<sup>35,54</sup> as well as binding<sup>50</sup> of IDPs. The computational protocol has been described in detail elsewhere.<sup>35,54,57,98</sup> Electrostatic interactions are treated using the PPPM method<sup>106</sup> implemented in the HOOMD package. For our simulation of polymers (polyampholytes) and dipoles,  $n_p = 100$  polymer chains are first randomly placed in a relatively large simulation box of dimensions  $40a \times 40a \times 40a$ . This system is energy-minimized for a period of  $500\tau$  with a timestep of  $0.001\tau$ , where  $\tau \equiv \sqrt{ma^2/\varepsilon}$  with  $m$  being the mass of each monomer bead. For simplicity, similar to the models in ref. 57, all monomer beads making up the polyampholyte chains and the dipole dimers are assigned the same mass. The initial equilibration is then performed for a period of  $1,000\tau$  at  $T^* = 4.0$ . The reduced temperature  $T^* \equiv k_B T/\varepsilon$ , where  $k_B$  is Boltzmann constant and  $T$  is absolute temperature, contains a factor of  $\epsilon_r$  via the above definition for  $\varepsilon$ . For direct comparisons of temperatures in different dielectric environments on the same footing, however, it is often useful to use the vacuum reduced temperature ( $T^*$

for  $\epsilon_r = 1$ ), denoted in the present work as

$$T_0^* \equiv \frac{T^*}{\epsilon_r} = \frac{4\pi\epsilon_0 k_B T a}{e^2}. \quad (12)$$

The velocity-Verlet algorithm is utilized to propagate the equations of motion. Periodic boundary conditions are applied to all three dimensions. The system is then compressed isotropically at  $T_0^* = 4.0$  for  $5,000\tau$  using linear scaling to a sufficiently higher density of  $\sim 0.73m/a^3$  by confining the polymers to a box of size  $19a \times 19a \times 19a$ . We next expand the box 15 times along one of the spatial dimensions (labeled as  $z$ ) at a much lower temperature of  $T_0^* = 0.5$ , resulting in final box dimensions of  $19a \times 19a \times 285a$ . After this procedure, the system is equilibrated for  $1,000\tau$  at the same  $T_0^* = 0.5$  using Langevin dynamics with a weak friction coefficient of  $0.1m/\tau$  (ref. 98). The Packmol package<sup>107</sup> is subsequently used to insert  $n_w = 12,000$  dipoles into the simulation box while keeping the positions of all the polymer beads fixed.<sup>86</sup> During the insertion process, a suitable distance criterion is set to avoid steric repulsion. After inserting the dipoles, we equilibrate the system again for a longer period of  $30,000\tau$  at several desired temperatures  $T_0^* \geq 3.0$  at which the dipoles are dynamic and well dispersed throughout the simulation box. At lower temperatures ( $T_0^* < 2.5$ ), we observe that the dipoles do not move much over extended periods of time—they appear to be essentially frozen—and thus are not a good model for liquid solvent. For this reason,  $T_0^* < 3.0$  is not used for production runs. Finally, each subsequent production run for  $T_0^* \geq 3.0$  is for a duration of  $100,000\tau$ , during which snapshots are saved every  $10\tau$  for the determination of various ensemble properties, including density profiles of polymers and dipoles in the simulation box. Coexistence curves (phase diagrams) of the polymers are determined from the polymer density distributions as described before.<sup>57</sup> Density of dipoles ( $\rho_w$ ) and density of polyampholytes ( $\rho$ ) are reported by the number densities of monomer beads in the two types of molecules, respectively, in units of  $1/a^3$ .

For the study of pure polymers, i.e., implicit-solvent systems of polyampholytes with no dipoles, the procedure is identical to that in ref. 57, viz.,  $n_p = 500$  polymer chains are initially placed randomly in a cubic box of length  $70a$ . After energy minimization and initial equilibration, this box is compressed to a cubic box of length  $33a$ . The simulation box for the system is then expanded eight times along one of the axes (named  $z$  as before)<sup>57</sup> to reach a final dimensions of  $33a \times 33a \times 264a$ . As for the polymer plus dipole simulations described above, equilibration is performed under periodic boundary conditions in the expanded box for  $30,000\tau$ , which is then followed by a production run for  $100,000\tau$  with snapshots saved every  $10\tau$  for subsequent analysis. Further details regarding simulation temperatures and boundary conditions are provided in ref. 57.

For the study of pure dipole solvent, i.e., systems that contain dipoles but no polymers, the main purpose of the simulations is to determine the effective relative permittivity of

bulk solvent as modeled by the dipoles under various conditions. We use  $n_w = 10,000$  dipoles for each simulation. The size of the cubic periodic simulation box is adjusted to model different dipole densities ( $\rho_w$ ). We first focus on  $\rho_w = 0.205$  and  $\rho_w = 0.252$ , which we deem sufficiently dense to exhibit liquid-like characteristics but not too dense to render the systems computationally intractable. The length of the cubic boxes utilized for these simulations are  $46a$  and  $43a$  respectively. The simulations are conducted for a broad range of temperatures, namely  $T_0^* = 3.0, 4.0, 5.0, 6.0, \text{ and } 7.0$ , as well as for a broad range of dipole moments, with  $q_d = \pm 1, \pm 2, \pm 3, \pm 4, \text{ and } \pm 5$ . To probe the dependence of the effective relative permittivity on both density and temperature, we further fix  $q_d = \pm 3$ , vary  $\rho_w$  from 0.205 to  $\approx 0.55$  at intervals of  $\approx 0.05$  ( $\rho_w = 0.205, 0.252, 0.301, 0.350, 0.401, 0.451, 0.500, \text{ and } 0.552$ ), and simulate every system for five temperatures from  $T_0^* = 3.0$  to 7.0 as above. Lastly, to arrive at a set of conditions to maintain a constant  $\rho_w$  as well as a temperature-independent effective relative permittivity, we fix  $\rho_w = 0.252$  and use theoretically fitted values of  $q_d$  (see below) to conduct simulations at  $T_0^* = 3.0, 4.0, 5.0, 6.0, 7.0, \text{ and } 8.0$  (the corresponding lengths of the cubic simulation boxes, in units of  $a$ , are: 46.0, 43.0, 40.5, 38.5, 36.8, 35.4, 34.2, and 33.1). For every simulation described above, we first energy-minimize to rid the system of significant steric clashes for a duration of  $100\tau$ , then equilibrate the system at the desired temperature using Langevin dynamics with the same low friction coefficient of  $0.1m/\tau$  for  $500\tau$ . The subsequent production run is performed for  $4,000\tau$  and snapshots are collected every  $1.0\tau$  for analysis.

As noted above, we use the same friction coefficient for explicit- and implicit-solvent systems. Equilibrium properties such as phase coexistence of the present explicit-chain models are independent of the choice of Langevin friction coefficient because friction coefficients affect dynamics but not thermodynamic distributions.

## RESULTS

**Effective Permittivities Of Pure Dipole Solvents.** We begin by determining baseline dielectric constants of the bulk solvents in our model by conducting simulations of pure dipole systems under a variety of conditions as outlined above, utilizing the following expression for the effective relative permittivity:<sup>35,68</sup>

$$\epsilon_r = 1 + \frac{\langle \mathbf{M}_T \cdot \mathbf{M}_T \rangle - \langle \mathbf{M}_T \rangle \cdot \langle \mathbf{M}_T \rangle}{3\Omega\epsilon_0 k_B T} \quad (13)$$

where  $\mathbf{M}_T$  is the total dipole moment vector and  $\Omega$  is the volume of the system, and  $\langle \dots \rangle$  represents averaging over the simulated ensemble, effectuated here by averaging over snapshots. The total dipole moment is given by  $\mathbf{M}_T = e \sum_i q_i \mathbf{R}_i$ , where the summation is over monomer beads of the system/subsystem of interest;  $q_i$  and  $\mathbf{R}_i$  are, respectively,

the charge and position vector of the  $i$ th bead. Our primary focus here is the dielectric contribution from the dipole solvents, in which case the summation is over the beads of the dipole dimers. In situations where the contribution from the polyampholytes to the dielectric environment is also taken into consideration, the summation would encompass all monomer beads in the system. (Note that the magnitude  $M_T$  in Eq. S12 of ref. 35 for  $\epsilon_r$  should be replaced by the vector  $\mathbf{M}_T$ .)

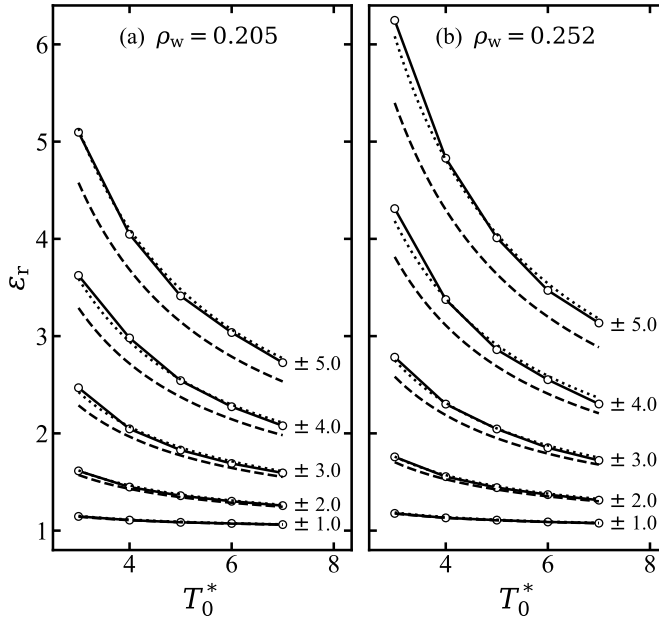


**Fig. 2:** Effective relative permittivity of pure dipoles as a model of polar solvent. Effective  $\epsilon_r$  is calculated by Eq. 13 with  $\rho_w = 0.205$  (a) and  $0.252$  (b) for dipoles with the indicated  $q_d$  values (shown as  $\pm|q_d|$  next to the curves) as functions of reduced temperature  $T_0^*$ . Solid lines connecting the simulated data points (circles) are merely a guide for the eye. Dashed curves representing Eq. 14 are for idealized uncorrelated dipoles. Dotted curves show the empirical fit for the different  $|q_d|$  values by Eq. 15.

Fig. 2 shows the variation of effective relative permittivity of pure dipole solvents with respect to dipole density ( $\epsilon_r$  for  $\rho_w = 0.205$  and  $0.252$  are compared), temperature  $T_0^*$ , and the charges  $q_d$  on the dipoles that make up the model polar solvent. As expected, since  $\epsilon_r$  is positively correlated with the ease at which the solvent can be polarized, the simulated data in Fig. 2 indicate that  $\epsilon_r$  increases with increasing  $|q_d|$  and  $\rho_w$ . This is because that corresponds to having stronger charges on the dipoles (hence a larger dipole moment  $\mu \approx |q_d|a$ ) and the presence, in a given volume, of a larger number of dipoles whose orientations can be perturbed by introducing other charges into the system. As  $T_0^*$  increases, however,  $\epsilon_r$  decreases because biased distributions of dipole orientations are disfavored by thermal agitation, as reflected partly by the  $1/T$  dependence of the second term in Eq. 13.

Inasmuch as the orientations of dipoles can be assumed to be uncorrelated, the analytical

formula

$$\epsilon_r = 1 + \frac{4\pi l_B \mu^2}{3} \left( \frac{\rho_w}{2} \right), \quad (14)$$

where  $l_B = e^2/(4\pi\epsilon_0 k_B T)$  is the vacuum Bjerrum length and  $(\rho_w/2)$  is the number density of dipoles (because  $\rho_w$  is defined to count two monomer beads per dipole as stated above), applies for a collection of fixed dipoles with  $\mu$  being the magnitude of the individual dipole moment (see, e.g., refs. 92, 108). This formula does not provide a sufficiently accurate description of our simulation data (dashed curves in Fig. 2), however, because although the magnitude of the dipole moment for a given  $|q_d|$  in our model may be considered practically fixed at  $\mu = |q_d|a$  because of the stiff spring constant  $K_{\text{bond}}$ , the orientations of the dipoles are correlated to a degree because of inter-dipole electrostatic interactions. As expected, the correlation among dipole orientations increases with increasing  $|q_d|$ , leading to larger mismatches seen in Fig. 2 between the simulated  $\epsilon_r$  data points and the dashed curves representing Eq. 14. Nonetheless, we find that the following empirical formula, which takes a form similar to Eq. 14 but with an extra multiplicative factor linear in  $\mu$ , viz.,

$$\epsilon_r = 1 + \frac{4\pi l_B \mu^2}{3} \left( \frac{\rho_w}{2} \right) (C_1 + C_2 \mu) \quad (15)$$

is capable of providing a reasonably good global fit for all the simulated  $\epsilon_r$  values in Fig. 2 (dotted curves) when  $C_1 = 1.0321441$  and  $C_2 = 0.02471877$ , thus enabling estimation of  $\epsilon_r$  values of dipole systems beyond those we have directly simulated.

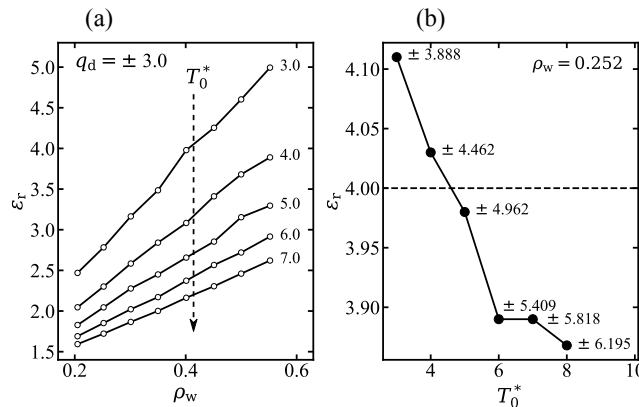


**Fig. 3:** Dependence of effective relative permittivity of model dipole solvent on density, dipole moment, and temperature. (a) Variation of effective  $\epsilon_r$  (Eq. 13) with respect to dipole density  $\rho_w$  and reduced temperature  $T_0^*$  (marked on the right of the curves) for dipoles sharing the same  $|q_d| = 3.0$ . The vertical dashed arrow across the curves indicates increasing temperature. (b) At constant  $\rho_w = 0.252$ , computed effective  $\epsilon_r$  (Eq. 13) for  $q_d$ 's estimated by Eq.15 ( $q_d$  values indicated beside simulated data points) to result in an essentially constant  $\epsilon_r \approx 4.0$  (marked by dashed horizontal line) at different temperatures (horizontal scale for  $T_0^*$ ). Note that the vertical scale covers only a narrow range of  $\epsilon_r$  from  $\approx 3.85$  to  $\approx 4.10$ . Solid lines connecting the simulated data points (circles in (a) and (b)) are merely a guide for the eye.

Further data in Fig. 3a on the dependence of simulated  $\epsilon_r$  value on temperature and dipole density  $\rho_w$  suggest an approximate linear relationship between  $\epsilon_r$  and  $\rho_w$ . Consistent with the observation above that the dipoles are well dispersed, and therefore fluid-like, for  $T_0^* \geq 3.0$ , the variation of  $\epsilon_r$  with  $\rho_w$  and  $T_0^*$  is smooth in this set of simulations. Making use of the trend in Fig. 3a and the empirical Eq. 15, we obtain a set of  $\mu$  values for dipole solvents that would maintain an essentially constant  $\epsilon_r$  over a range of different temperatures (Fig. 3b). Because  $\epsilon_r$  for dipoles with a constant  $\mu$  decreases with increasing  $T_0^*$  (Fig. 2),  $\mu$  has to increase with increasing  $T_0^*$  to maintain an essentially temperature-independent  $\epsilon_r$  (Fig. 3b). We will use these  $\mu$  values to construct temperature-independent solvent dielectric environments for the simulation study of polyampholyte LLPS below.

**Phase Behaviors Of Polyampholytes In Dipole Solvent.** With the baseline effective relative permittivities of dipole models of polar solvent established, we now turn to LLPS behaviors of the polyampholyte chains immersed in these model solvent molecules. For most of these studies, we set the effective bulk-solvent  $\epsilon_r \approx 4.0$ . This relatively small  $\epsilon_r$  is chosen for computational tractability. We refrained from assigning highly positive and negative charges to the model solvent molecules or having very high densities of these molecules in the model solvent. Both of these features would increase effective  $\epsilon_r$  but would decrease sampling efficiency. As shown below, insights are gained by the present model into physical principles regarding electrostatics-driven LLPS in polar solvent,  $\epsilon_r \approx 4.0$  being much smaller than  $\epsilon_r \approx 80$  for water notwithstanding.

Fig. 4 is an overview of our polyampholytes-and-dipoles systems, showing the density profiles of the polyampholytes and the dipoles for the three sequences sv15, sv20, and sv30, each at four different simulation temperatures. A condensed polyampholyte-rich droplet, corresponding to a local peak in polymer bead density  $\rho$  (red curves), is seen in every panel of this figure. Expectedly, each of these droplets coincides with a local minimum in dipole density (blue curves). As temperature increases from top to bottom in Fig. 4, effects of configurational entropy gain in significance. Consequently, the packing of polyampholytes in the droplet loosens up (lower and broadened peak, red curves) and a concomitant relative increase in dipole density ensues (shallower but wider dip, blue curves). In other words, more solvent molecules reside in the polyampholyte-rich phase as temperature increases.

Fig. 4 shows further that the effective  $\epsilon_r$  contributed by the dipole solvent decreases inside the polyampholyte-rich droplet (dips along green curves at  $z$ -positions of the droplets), tracking the decrease in  $\rho_w$ . The  $z$ -dependent relative permittivity in Fig. 4 is computed using the formulation in ref. 109 for “slab geometry” in which one spatial dimension ( $z$ ) is distinct from the other two spatial dimensions ( $x, y$ ). The  $\epsilon_r(z)$  plotted in Fig. 4 is the component of the diagonal permittivity tensor parallel to the latter two dimensions i.e., the

$x$ - $x$ , or equivalently the  $y$ - $y$  component, given by the expression

$$\epsilon_{r\parallel}(z) = 1 + \frac{1}{2\epsilon_0 k_B T} \left[ \langle \mathbf{m}_{\parallel}(z) \cdot \mathbf{M}_{T\parallel} \rangle - \langle \mathbf{m}_{\parallel}(z) \rangle \cdot \langle \mathbf{M}_{T\parallel} \rangle \right] \quad (16)$$

where the two-dimensional vectors  $\mathbf{m}_{\parallel}(z)$  and  $\mathbf{M}_{T\parallel}$  are both confined to the  $x$ - $y$  plane.  $\mathbf{m}_{\parallel}(z)$  is the  $x$ - $y$  component of the local dipole moment density (dipole moment within the local volume sampled divided by the local volume) and  $\mathbf{M}_{T\parallel}$  is the  $x$ - $y$  component of the dipole moment of the entire system, and  $\langle \dots \rangle$  denotes averaging over snapshots (Eq. 13 of ref. 109). Note that expressions for local  $\epsilon_r$  involves not only local but also global dipole moments,<sup>109-111</sup> and Eq. 13 can be recovered from Eq. 16 by recognizing that  $\mathbf{m}_{\parallel}(z) \rightarrow \mathbf{M}_{T\parallel}/\Omega$  when the sampling volume for  $\mathbf{m}_{\parallel}(z)$  encompasses the total volume  $\Omega$ , and that when the system is isotropic after subtracting an overall average dipole moment  $\langle \mathbf{M}_{T\parallel} \rangle$ ,  $\langle |\mathbf{M}_{T\parallel} - \langle \mathbf{M}_{T\parallel} \rangle|^2 \rangle = (2/3) \langle |\mathbf{M}_T - \langle \mathbf{M}_T \rangle|^2 \rangle$ . In our calculation of  $\mathbf{m}_{\parallel}(z)$ , we consider the dipoles in slices of thickness  $10a$  in the  $z$ -direction, and include only those dipoles whose centers of mass are inside the bin. The  $z$ - $z$  component of the permittivity tensor—the orthogonal component—may also be obtained and is expected to yield values similar to that given by Eq. 16; but the more limited statistics available to this calculation due to the restriction to one spatial dimension may present computational challenges.<sup>109</sup> For this reason we do not pursue it here, while recognizing that Fig. 4, as it stands, illustrates reasonably well that the solvent dielectric environment experienced by polyampholyte chains inside the condensed droplet can be quite different from that outside in the dilute phase.

At temperatures significantly higher than those simulated in Fig. 4, condensed droplets disassemble. An example is provided by the snapshots in Fig. 5 for sequence sv20 at two temperatures. Consistent with the  $\rho_w$  profiles in Fig. 4, at a moderate temperature of  $T_0^* = 5.5$ , Fig. 5a-c show that although a condensed polyampholyte droplet is in place, a substantial number of dipole solvent molecules are found inside the droplet.

Using methods described above and in previous studies,<sup>35,54,57,98</sup> we determine the phase diagrams for sequences sv15, sv20, and sv30, each using five different solvent models (Fig. 6). The upper critical solution temperature ( $T_{0,\text{cr}}^*$ )—above which phase separation is impossible—is estimated for each system (Table 1). When comparison is made across different sequences, LLPS propensity is seen to increase from sv15 to sv20 to sv30 for all five solvent models, as quantified by a monotonic increase in  $T_{0,\text{cr}}^*$  from left to right for every row in Table 1, consistent with and generalizing previous findings that LLPS propensity tend to increase with increasingly negative values<sup>46,50</sup> of the SCD charge pattern parameter.<sup>48,55,57,61</sup>

As far as solvent model is concerned, Fig. 6 compares three explicit-solvent models [(i), (ii), and (iii)] and two implicit-solvent models [(iv) and (v)]. The implicit-solvent model results for sv20 are simulated here anew, those for sv15 and sv30 are taken from ref. 57. Between these two models, the lower LLPS propensity of model (v) than model (iv)—for

all three sequences—follows directly from the definition that the LLPS-driving effective electrostatic interactions among the polyampholyte chains are weakened by a factor of  $\epsilon_r = 4.0$  in model (v) than in model (iv).

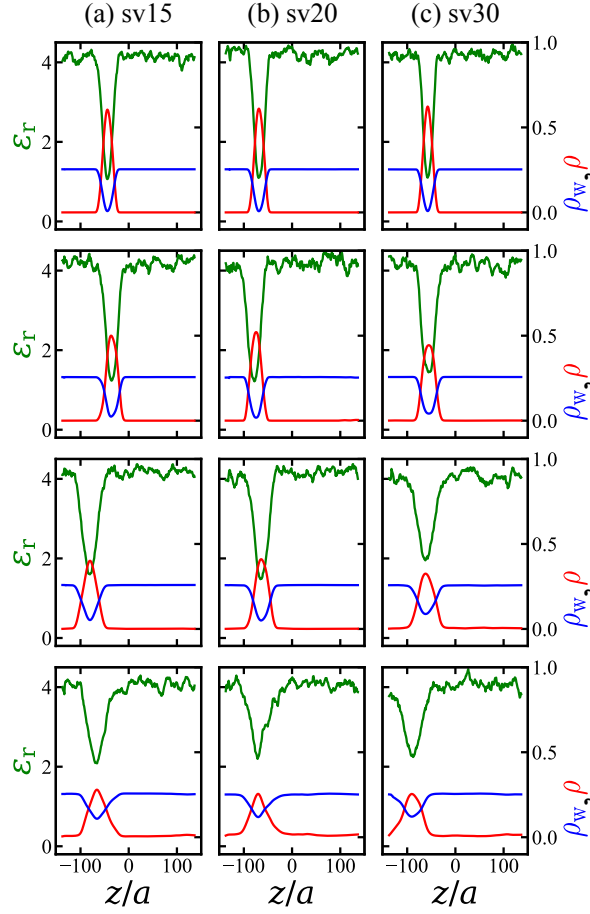


**Fig. 4:** Density and dielectric profiles of phase-separated polyampholytes in dipole solvents. Simulation results for systems each containing  $n_p = 100$  polyampholyte chains and  $n_w = 12,000$  dipoles are shown for sequences (a) sv15, (b) sv20, and (c) sv30 at temperatures (top to bottom)  $T_0^* = 3.0, 4.0, 5.0,$  and  $5.5$  (a),  $T_0^* = 3.0, 4.0, 5.0,$  and  $6.0$  (b), and  $T_0^* = 3.0, 5.0, 6.0,$  and  $6.5$  (c), respectively. Densities of dipoles ( $\rho_w$ , blue curves) and polyampholytes ( $\rho$ , red curves) as a function of the horizontal coordinate  $z$  of the simulation box are given by the vertical scale on the right, with  $\rho_w \approx 0.252$  outside of the polyampholyte-rich droplet (peak region of the red curve) in every case. Local effective relative permittivity  $\epsilon_r(z)$  arising from the dipole molecules (green curves, vertical scale on the left) is calculated by using Eq. 16 for  $\epsilon_{r\parallel}(z)$ . The  $\rho_w(z)$ ,  $\rho(z)$ , and  $\epsilon_r(z)$  profiles are computed by averaging over successive bins of width  $10a$  and plotting the averages at the midpoint of each bin. The effective  $\epsilon_r$  for bulk dipole solvent is maintained at an essentially constant value of  $\approx 4.0$  at different  $T_0^*$ s for all the systems considered in this figure by using the  $q_d$  values in Fig. 3b and  $q_d = \pm 5.191$  for  $T_0^* = 5.5$  and  $q_d = \pm 5.618$  for  $T_0^* = 6.5$ .

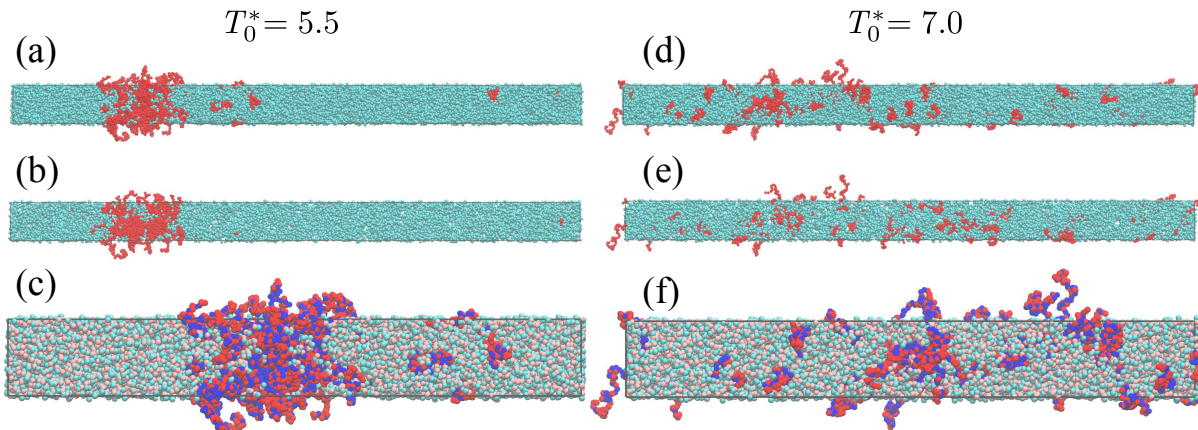


**Fig. 5:** Polyampholyte phase separation in explicit dipole solvent. Snapshots of  $n_p = 100$  sv20 polyampholyte chains and  $n_w = 12,000$  dipoles depict a phase-separated condensed polyampholyte-rich droplet at low temperature ( $T_0^* = 5.5$ , left column, (a)–(c)) and a lack of phase separation at a higher temperature ( $T_0^* = 7.0$ , right column, (d)–(f)). Chains and dipoles at the boundaries of the periodic simulation boxes are unwrapped. (a) and (d) show an overview of the entire simulation box, whereas (b) and (e) show a cross-sectional view of a thin slice parallel to the page. (c) and (f) are enlarged views of the left halves of (a) and (d), respectively. In (a), (b), (d), and (e), polyampholytes are depicted in red, and dipole solvent molecules are depicted in cyan. In (c) and (f), the positively and negatively charged beads in the polyampholytes are in blue and red, whereas the positively and negatively charged beads in the dipoles are in cyan and pink, respectively (same color code as that in Fig. 1).

The LLPS propensities of the present explicit-solvent models are all substantially higher than that of the corresponding implicit-solvent models for the same sequence because, by construction, the non-electrostatic LJ-like part of dipole-polyampholyte interactions is purely repulsive (Eqs. 6 and 7). These repulsive interactions, probably in conjunction with related configurational entropy effects, amount to a hydrophobicity-like,<sup>112</sup> general solvophobic driving force<sup>113</sup> against solvation of the polyampholytes in the dilute phase and thus favoring their condensation. While this feature may be viewed as artifactual, as the LJ-like interactions of realistic water models are not purely repulsive and thus engender more subtle solvation effects, the large offset between the coexistence curves of implicit-solvent and explicit-solvent models in Fig. 6 is largely inconsequential to the questions of physical principle at hand. As argued below, it is appropriate for the present purpose to focus our comparison on LLPS properties of the explicit-solvent models.

Among the three explicit-solvent models in Fig. 6, the LLPS propensity of model (i) is always higher than that of model (iii) because they share the same nonpolar solvent (“dipoles” with their charges switched off) but LLPS-driving electrostatic interactions among the polyampholytes are weakened by a factor of  $\epsilon_r = 4.0$  for model (iii) relative to model (i). In this respect, comparison between models (i) and (iii) is similar to the comparison between models (iv) and (v).

**Table 1.** Upper Critical Solution Temperature  $T_{0,\text{cr}}^*$  for Polyampholyte LLPS Simulated Using Different Solvent Models in Fig. 6. Values of the SCD Sequence Charge Pattern Parameter<sup>46</sup> for the Sequences<sup>45</sup> sv15, sv20, and sv30 are Provided in Parentheses.

solvent model	sv15 (SCD = $-4.35$ )	sv20 (SCD = $-7.37$ )	sv30 (SCD = $-27.8$ )
(i)	6.2	6.6	7.1
(ii)	5.7	6.2	7.0
(iii)	5.8	5.9	6.3
(iv)	3.9	4.0	5.0
(v)	3.6	3.6	3.8

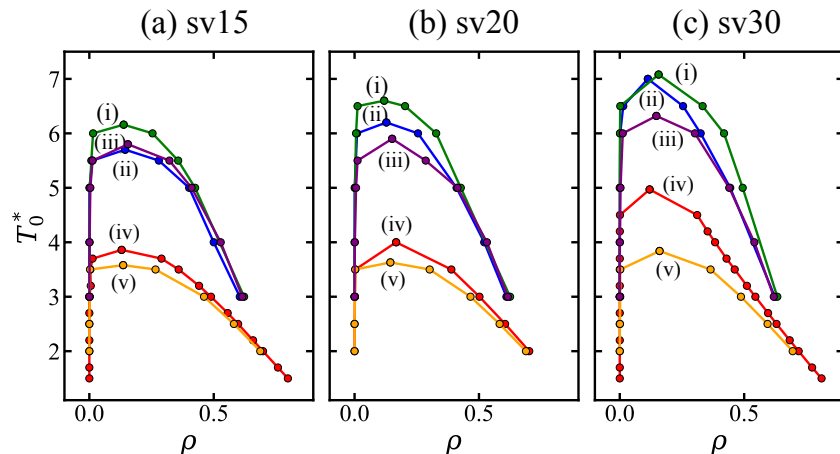


**Fig. 6:** Phase diagrams of polyampholytes in implicit solvents and explicit dipole and nonpolar solvents. Coexistence curves (i), (ii), and (iii) for sequences sv15 (a), sv20 (b), and sv30 (c) are determined by simulations of systems each consisting of  $n_p = 100$  polyampholyte chains and  $n_w = 12,000$  dipoles ( $|q_d| > 0$ ) or uncharged dimers ( $q_d = 0$ ). The charges  $q_d$  on the dipoles at different temperatures are adjusted by Eq. 15 such that the effective relative permittivity arising from the dipoles are essentially constant, at  $\epsilon_r \approx 4.0$ , for all temperatures. Corresponding coexistence curves (iv) and (v), determined by implicit-solvent simulations (no explicit solvent molecules) using  $n_p = 500$  polyampholyte chains,<sup>57</sup> are included for comparison.  $T_0^*$  is vacuum reduced temperature,  $\rho$  is density of polyampholyte monomer beads in units of  $1/a^3$ . Lines joining computed data points (circles) are merely a guide for the eye. The five different solvent models [(i)–(v)] are: (i) Explicit nonpolar solvent, i.e., “dipoles” with  $q_d = 0$ ,  $\epsilon_r = 1$  for polyampholyte electrostatics (green curves). (ii) Explicit dipole solvent, with different  $|q_d| > 0$  for different  $T_0^*$  to maintain an essentially  $T_0^*$ -independent effective bulk-solvent  $\epsilon_r \approx 4.0$ ,  $\epsilon_r = 1$  for all electrostatic interactions (blue curves). (iii) Explicit nonpolar solvent, same as (i) but  $\epsilon_r = 4.0$  is used for polyampholyte electrostatics (magenta curves). (iv) Implicit-solvent,  $\epsilon_r = 1$  (red curves). (v) Implicit-solvent,  $\epsilon_r = 4.0$  (orange curves). The highest  $T_0^*$  value of a coexistence curve for a given system is its upper critical solution temperature  $T_{0,\text{cr}}^*$ . The  $T_{0,\text{cr}}^*$  values for all the systems considered in this figure are provided in Table 1.

For our purpose, the most physically informative comparison in Fig. 6 is between model (ii) and model (iii). The two models share the same repulsive LJ-like polyampholyte-solvent interactions, which serve as a baseline for comparing, on one hand, the LLPS behavior of polyampholytes immersed in explicit dipole solvent molecules with dipole charges tuned to provide an essentially temperature-independent effective bulk-solvent  $\epsilon_r \approx 4.0$  with all charges in the system interacting via the full Coulomb potential, and on the other hand, the LLPS behavior of polyampholytes immersed in nonpolar solvent molecules interacting via a Coulomb potential with strength reduced by  $\epsilon_r = 4.0$ . At a conceptual level, this comparison serves to assess the accuracy, or potential pitfall, of the common practice of using the bulk-water  $\epsilon_r$  in implicit-solvent simulations of LLPS,<sup>39,44,52,54–56,58,60</sup> although the temperature dependence of implicit-solvent effective interactions<sup>39,40</sup> and bulk-water  $\epsilon_r$  (which varies from  $\approx 88.7$  to  $55.7$  from  $0^\circ$  to  $100^\circ\text{C}$ )<sup>114</sup> should also be taken into account in real-world applications.

Comparisons between the blue (ii) and magenta (iii) curves in Fig. 6 indicate that there is, in general, an appreciable difference in predicted LLPS properties between the two approaches. The observed differences are not large. It can be very minor for the sequence with a low  $-\text{SCD}$  value (sv15) but are larger for the sequence with a high  $-\text{SCD}$  value (sv30). The critical temperature  $T_{0,\text{cr}}^*$  for the model with explicit dipole solvent molecules and full electrostatic interactions (blue curve) is higher than the corresponding  $T_{0,\text{cr}}^*$  for the model with nonpolar solvent molecules but reduced electrostatic interactions (magenta curve) for sv20 and sv30. However, the reverse is true for sv15, albeit the difference in this case is very small. Taken together, these observations suggest that although there is a tendency for implicit-solvent simulations of LLPS using bulk-water  $\epsilon_r$  to underestimate LLPS propensity, there is no absolute rule against it giving a small overestimation of LLPS propensity, as that may well depend on the structural and energetic details of the system.

**Analytical Theory of Pure Dipole Solvent Systems.** To assess the generality of the above observations from molecular dynamics simulations, we have also developed corresponding analytical theories that treat both polyampholyte and dipole degrees of freedom, paying particular attention to excluded volume effects of the polyampholyte chains and the dipoles as model solvent molecules. Analytical formulations are useful for conceptual understanding and hypothesis evaluation. As a theoretical tool, they are complementary to molecular dynamics simulations. Although analytical theories lack the structural and energetic details of molecular dynamics models, computation needed for numerical solutions to analytical formulations such as RPA<sup>35,53</sup> and field-theoretic simulations (FTS)<sup>61–64</sup> are often significantly more efficient than molecular dynamics simulations, thus allowing more physically informative variations in modeling setup to be explored.

As for the explicit-chain, explicit-solvent simulation study above, our analytical devel-

opment begins with the baseline case of pure dipoles as a model of polar solvents. Consider a system of volume  $\Omega$  containing  $n_w$  dipoles subject to a local incompressibility condition to account for dipole excluded volume,

$$\rho_w(\mathbf{r}) = \frac{1}{v}, \quad (17)$$

where  $\rho_w(\mathbf{r})$  is the number density at the spatial position  $\mathbf{r}$  and  $v$  is the volume assigned to each dipole. (Note that each dipole is counted once by the  $\rho_w$  here whereas the bead density for the dipoles in the molecular dynamics simulations, denoted by the same symbol  $\rho_w$ , counts each dipole twice because it contains two beads; hence the  $\rho_w$  value in the present analytical theory formulation is equivalent to  $(\rho_w/2)$  in the molecular dynamics results reported above). With only dipoles in the system,  $v^{-1} = n_w/\Omega$ . We let  $\mathbf{r}_i$  and  $\boldsymbol{\mu}_i$  denote the position and dipole moment of individual dipole  $i$ , and model each dipole as a soft sphere following a Gaussian distribution  $\Gamma(\mathbf{r})$  of width  $\bar{a}$ . The local number density  $\rho_w(\mathbf{r})$  and dipole moment density  $\mathbf{m}(\mathbf{r})$  (i.e. the polarization) can then be re-expressed in their respective smeared forms:

$$\rho_w(\mathbf{r}) = \sum_{i=1}^{n_w} \Gamma(\mathbf{r} - \mathbf{r}_i) \quad (18a)$$

$$\mathbf{m}(\mathbf{r}) = \sum_{i=1}^{n_w} \boldsymbol{\mu}_i \Gamma(\mathbf{r} - \mathbf{r}_i) \quad (18b)$$

with the Gaussian smearing function  $\Gamma(\mathbf{r}) = \exp(-\mathbf{r}^2/2\bar{a}^2)/(2\pi\bar{a}^2)^{3/2}$ . This smearing procedure was introduced in ref. 115 and is a convenient way of handling ultraviolet (short-distance) divergences arising from point interactions. A spatially varying  $\mathbf{m}(\mathbf{r})$  gives rise to a bound charge density  $\rho_c(\mathbf{r}) = -\nabla \cdot \mathbf{m}(\mathbf{r})$ . We consider two distinct cases where the dipoles are either given freely orientable dipole moments of fixed, i.e., permanent, magnitude,  $|\boldsymbol{\mu}_i| = \mu$  (“fixed dipoles”), or where every dipole is associated with a harmonic energy contribution  $\kappa_d \boldsymbol{\mu}_i^2/2$  (“polarizable dipoles”) where  $\kappa_d$  is the corresponding spring constant.

The canonical partition function for this system is

$$\mathcal{Z} = \frac{1}{n_w!} \prod_{i=1}^{n_w} \int d\mathbf{r}_i \int d\boldsymbol{\mu}_i e^{-\mathcal{U}} \delta \left[ \rho_w(\mathbf{r}) - \frac{1}{v} \right], \quad (19)$$

where the functional  $\delta$ -function implements the incompressibility condition in Eq. 17 and  $\mathcal{U}$  is the Hamiltonian. In the case of fixed dipoles, the integrations over  $\boldsymbol{\mu}_i$  are reduced to

solid angle integrals, and  $\mathcal{U}$  is the total electrostatic potential energy,

$$\mathcal{U} = \frac{1}{2\Omega} \sum_{\mathbf{k} \neq \mathbf{0}} \hat{\rho}_c(\mathbf{k}) \frac{4\pi l_B}{\mathbf{k}^2} \hat{\rho}_c(-\mathbf{k}) = \frac{l_B}{2} \int d\mathbf{r} \int d\mathbf{r}' \frac{\rho_c(\mathbf{r})\rho_c(\mathbf{r}')}{|\mathbf{r} - \mathbf{r}'|} \quad (20)$$

where  $\hat{\rho}_c(\mathbf{k}) = i\mathbf{k} \cdot \hat{\mathbf{m}}(\mathbf{k})$  is the Fourier transform of  $\rho_c(\mathbf{r})$ ,  $l_B$  is the vacuum Bjerrum length as defined above, and  $i^2 = -1$ . Note that the  $\mathbf{k} = \mathbf{0}$  mode can be dropped in the above summation because overall charge neutrality of the system entails  $\hat{\rho}_c(\mathbf{k} = \mathbf{0}) = 0$ . In the case of polarizable dipoles,  $\mathcal{U}$  contains the additional term  $\sum_{i=1}^{n_w} \beta \kappa_d \boldsymbol{\mu}_i^2 / 2$  where  $\beta \equiv 1/k_B T$ .

A formula for the relative permittivity  $\epsilon_r$  arising from the dipoles can be obtained by imagining adding a small test charge to the system and looking at the induced electrostatic potential far away from the test charge. As derived in ref. 116, this consideration yields a relation between  $\epsilon_r$  and the charge-charge correlation function:

$$\frac{1}{\epsilon_r} = \lim_{\mathbf{k} \rightarrow \mathbf{0}} \left( 1 - \frac{4\pi l_B}{\mathbf{k}^2 \Omega} \langle \hat{\rho}_c(\mathbf{k}) \hat{\rho}_c(-\mathbf{k}) \rangle \right), \quad (21)$$

where  $\langle \dots \rangle$  denotes the thermal average over  $\{\mathbf{r}_i, \boldsymbol{\mu}_i\}$ .

Following a standard procedure using Hubbard-Stratonovich transformations,<sup>117,118</sup> the partition function in Eq. 19 can be turned into a statistical field theory where the  $\{\mathbf{r}_i, \boldsymbol{\mu}_i\}$  variables are traded in favor of charge- and number density conjugate fields  $\psi(\mathbf{r})$  and  $w(\mathbf{r})$ , leading to

$$\mathcal{Z} = \frac{\Omega^{n_w}}{n_w!} \int \mathcal{D}w \mathcal{D}\psi e^{-\mathcal{H}} \quad (22)$$

up to an inconsequential overall multiplicative constant, where

$$\mathcal{H}[w, \psi] = -n_w \ln \mathcal{Q}_w + \frac{1}{2\Omega} \sum_{\mathbf{k} \neq \mathbf{0}} \frac{\mathbf{k}^2}{4\pi l_B} \hat{\psi}(\mathbf{k}) \hat{\psi}(-\mathbf{k}) - \frac{i}{v} \hat{w}(\mathbf{0}), \quad (23)$$

and

$$\int \mathcal{D}w \mathcal{D}\psi = \prod_{\mathbf{k} \neq \mathbf{0}} \sqrt{\frac{\mathbf{k}^2}{4\pi l_B v}} \int d\hat{w}(\mathbf{k}) \int d\hat{\psi}(\mathbf{k}) \quad (24)$$

in  $\mathbf{k}$ -space representation, with  $\hat{\psi}(\mathbf{k})$  and  $\hat{w}(\mathbf{k})$  being the Fourier transforms, respectively, of  $\psi(\mathbf{r})$  and  $w(\mathbf{r})$ . The field Hamiltonian  $\mathcal{H}$  is thus expressed in terms of the Fourier transformed fields  $\hat{w}$  and  $\hat{\psi}$ . In Eq. 23,  $\mathcal{Q}_w$  is a single dipole partition function, whose form follows from the Hubbard-Stratonovich transformation.<sup>95</sup> It is

$$\mathcal{Q}_w = \frac{1}{\Omega} \int d\mathbf{r} \exp \left\{ -\frac{i}{\Omega} \sum_{\mathbf{k}} \hat{w}(\mathbf{k}) \hat{\Gamma}(-\mathbf{k}) e^{-i\mathbf{k} \cdot \mathbf{r}} \right\} \frac{\sinh \left[ (1/\Omega) \sum_{\mathbf{k} \neq \mathbf{0}} |\mathbf{k}| \mu \hat{\psi}(\mathbf{k}) \hat{\Gamma}(-\mathbf{k}) e^{-i\mathbf{k} \cdot \mathbf{r}} \right]}{(1/\Omega) \sum_{\mathbf{k} \neq \mathbf{0}} |\mathbf{k}| \mu \hat{\psi}(\mathbf{k}) \hat{\Gamma}(-\mathbf{k}) e^{-i\mathbf{k} \cdot \mathbf{r}}} \quad (25)$$

for fixed dipoles, and

$$\mathcal{Q}_w = \frac{1}{\Omega} \int d\mathbf{r} \exp \left\{ -\frac{i}{\Omega} \sum_{\mathbf{k}} \hat{w}(\mathbf{k}) \hat{\Gamma}(-\mathbf{k}) e^{-i\mathbf{k}\cdot\mathbf{r}} \right\} \exp \left\{ \frac{\left[ \sum_{\mathbf{k} \neq \mathbf{0}} \mathbf{k} \hat{\psi}(\mathbf{k}) \hat{\Gamma}(-\mathbf{k}) e^{-i\mathbf{k}\cdot\mathbf{r}} \right]^2}{2\beta\kappa_d\Omega^2} \right\} \quad (26)$$

for polarizable dipoles, where the Fourier-transformed smearing function  $\hat{\Gamma}(\mathbf{k}) = \exp(-\bar{a}^2\mathbf{k}^2/2)$ . The second factor in the integrands of Eqs. 25 and 26 (involving the sinh function in Eq. 25 and the exp function in Eq. 26) results from the dipole moment integrals  $\int d\hat{\mathbf{n}} \exp(-i\boldsymbol{\mu}\hat{\mathbf{n}} \cdot \nabla\check{\psi})$  (where  $\hat{\mathbf{n}}$  is the unit vector along the dipole moment) and  $\int d\boldsymbol{\mu} \exp(-\beta\kappa\boldsymbol{\mu}^2/2 - i\boldsymbol{\mu} \cdot \nabla\check{\psi})$ , respectively, with  $\check{\psi}(\mathbf{r}) \equiv \int d\mathbf{r}' \Gamma(\mathbf{r} - \mathbf{r}') \psi(\mathbf{r}')$ . For the case of fixed dipoles, the integral is most easily computed in the frame of reference where the  $z$ -component of  $\hat{\mathbf{n}}$  points along  $\nabla\check{\psi}$ . In calculating these integrals, overall multiplicative constants have been dropped as they are irrelevant for the computations that will follow. Recognizing that the charge-charge correlation function in Eq. 21 may be rewritten in a field-theory representation involving the correlation function of the  $\psi$  field,<sup>118</sup>

$$\frac{1}{\Omega} \langle \hat{\rho}_c(\mathbf{k}) \hat{\rho}_c(-\mathbf{k}) \rangle = \frac{\mathbf{k}^2}{4\pi l_B} \left[ 1 - \frac{\mathbf{k}^2}{4\pi l_B} \frac{\langle \hat{\psi}(\mathbf{k}) \hat{\psi}(-\mathbf{k}) \rangle}{\Omega} \right], \quad (27)$$

and substituting this expression into Eq. 21 leads to the field-theory expression for the relative permittivity,

$$\frac{1}{\epsilon_r} = \lim_{\mathbf{k} \rightarrow \mathbf{0}} \frac{\mathbf{k}^2}{4\pi l_B \Omega} \langle \hat{\psi}(-\mathbf{k}) \hat{\psi}(\mathbf{k}) \rangle, \quad (28)$$

where now  $\langle \dots \rangle$  denotes an average over field configurations weighted by  $\exp(-\mathcal{H})$ .

We next proceed to the calculation of this  $\psi$  correlation function in order to compute  $\epsilon_r$ . As a first approximation—which corresponds to RPA—we compute it analytically accounting only for Gaussian fluctuations in the fields. Introducing  $|\Psi(\mathbf{k})\rangle = [\hat{w}(\mathbf{k}), \hat{\psi}(\mathbf{k})]^T$ , where the superscript “T” denotes (vector) transposition, the field Hamiltonian in this approximation is

$$\mathcal{H} \approx \frac{1}{2\Omega} \sum_{\mathbf{k} \neq \mathbf{0}} \langle \Psi(-\mathbf{k}) | \hat{\Delta}(\mathbf{k}) | \Psi(\mathbf{k}) \rangle, \quad (29)$$

which contains only terms quadratic in the fields, and where

$$\hat{\Delta}(\mathbf{k}) \rightarrow \hat{\Delta}_k = \begin{pmatrix} \hat{\Gamma}_k^2/v & 0 \\ 0 & (k^2/4\pi l_B) \left( 1 + \chi_D \hat{\Gamma}_k^2 \right) \end{pmatrix} \quad (30)$$

with  $k = |\mathbf{k}|$ ,  $\hat{\Gamma}_k$  standing for  $\exp(-\bar{a}^2 k^2/2)$ , and

$$\chi_{\text{D}} = \begin{cases} \frac{4\pi l_{\text{B}} \mu^2}{3v} & \text{(fixed dipoles)} \\ \frac{4\pi K}{v} & \text{(polarizable dipoles)} \end{cases} \quad (31)$$

where  $K \equiv l_{\text{B}}/\beta\kappa_{\text{d}}$  is a temperature-independent factor corresponding to the molecular polarizability in our reduced units. When Eq. 28 is computed using the RPA Hamiltonian Eq. 29, the  $\psi$  correlation is simply the  $\psi\psi$  element of  $\hat{\Delta}^{-1}$ , which is equal to the reciprocal of the  $\psi\psi$  component of  $\hat{\Delta}$  (bottom-right element) in Eq. 30. It follows that

$$\epsilon_{\text{r}} = 1 + \chi_{\text{D}} \quad (32)$$

in RPA, yielding the standard formula in classical electrodynamics for uncorrelated dipoles. Eq. 32 with the  $\chi_{\text{D}}$  expression for fixed dipoles in Eq. 31 is equivalent to Eq. 14 for analyzing molecular dynamics simulation data on pure dipole systems in Fig. 2.

Going beyond RPA, we can calculate the  $\psi$  correlation function more accurately by using FTS on a lattice.<sup>119</sup> In FTS, the continuum fields  $w(\mathbf{r})$  and  $\psi(\mathbf{r})$  are approximated by discrete field variables defined on the sites of a cubic lattice with periodic boundary conditions. Due to the complex nature of  $\mathcal{H}$ , field averages (such as the  $\psi$  correlation function) are typically computed in FTS using the Complex-Langevin (CL) method,<sup>120,121</sup>—a technique inspired by stochastic quantization of field theories<sup>122–124</sup>—where a fictitious time coordinate is introduced such that  $w(\mathbf{r}) \rightarrow w(\mathbf{r}, t)$  and  $\psi(\mathbf{r}) \rightarrow \psi(\mathbf{r}, t)$  and the fields are now complex. The fields evolve in CL time according to the Langevin equation

$$\frac{\partial \varphi(\mathbf{r}, t)}{\partial t} = -\frac{\delta \mathcal{H}}{\delta \varphi(\mathbf{r}, t)} + \eta_{\varphi}(\mathbf{r}, t), \quad \varphi = w, \psi, \quad (33)$$

where  $\eta_{\varphi}$  is a real-valued Gaussian noise with zero mean and  $\langle \eta_{\varphi}(\mathbf{r}, t) \eta_{\varphi'}(\mathbf{r}', t') \rangle = 2\delta_{\varphi, \varphi'} \delta(\mathbf{r} - \mathbf{r}') \delta(t - t')$ . In the CL method, field averages can be shown to correspond to asymptotic CL time averages. In this work, we use the first order semi-implicit method of ref. 125 to solve Eq. 33 numerically.

Fig. 7 shows  $\epsilon_{\text{r}}$  computed by FTS for several representative parameter values. The FTS  $\psi$  correlation functions were computed on a  $24^3$  lattice with a lattice spacing  $\Delta x = \bar{a} = 1/\sqrt{6}$  and a time step  $\Delta t = 10^{-3}$ . After an initial equilibration period of  $2 \times 10^6$  time steps, the fields were sampled every 1,000 steps for  $\sim 8 \times 10^6$  steps. Fig. 7 shows the mean and standard deviation among three independent simulations that were performed for each value of  $l_{\text{B}}$ . All simulations used  $v = 0.1$ . The results for fixed dipoles were obtained for  $\mu = 0.2$  and  $\mu = 0.35$ . The polarizable dipoles were simulated using  $K = 0.151197$  which gives  $\epsilon_{\text{r}} = 20$  according to Eqs. 31 and 32. With the relative permittivity of the polymer material

set to unity in the following analytical theory development, the temperature-independent  $\epsilon_r$  value of 20 corresponds approximately to the ratio of the relative permittivities of  $\approx 80$  for water and  $\sim 4$  for proteins (see, e.g., refs. 29, 35, 51, 65 and Discussion below). For the parameters considered, Fig. 7 shows that the FTS results follow the RPA formulas in Eqs. 31 and 32 reasonably well.

It is instructive to compare our predicted  $l_B$ -independent  $\epsilon_r$  for polarizable dipoles in Fig. 7 to the results of a recent field-theoretic perturbation theory for polymers of polarizable beads.<sup>126</sup> Interestingly, while Figs. 8b and 9b of ref. 126 show that field fluctuations beyond Gaussian order affect the value of  $\epsilon_r$  for the compressible case ( $B = 1$  in the notation of their system) leading to an  $\epsilon_r$  that varies with  $l_B$ , their one-loop contribution to  $\epsilon_r$  vanishes for the incompressible case ( $B = \infty$ ) when there is only one kind of beads in the system (their  $\alpha_A = \alpha_B$ ) leading to an  $\epsilon_r$  essentially independent of  $l_B$  (Eq. 29 of ref. 126). Because our pure dipole systems is incompressible and the  $\alpha_A = \alpha_B$  case in ref. 126 is akin to our polarizable dipole system, the finding in ref. 126 that the one-loop contribution vanishes for  $\alpha_A = \alpha_B$ ,  $B = \infty$  provides additional rationalization for the observation in Fig. 7 of good agreement between RPA and FTS as well as an  $l_B$ -independent  $\epsilon_r$  for polarizable dipoles.

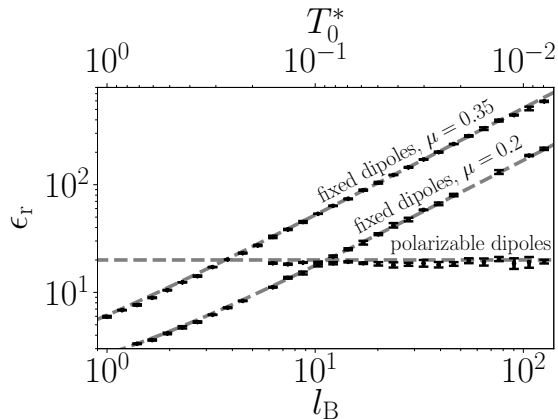


**Fig. 7:** Relative permittivity computed by FTS for incompressible pure dipoles. Each error bar indicates the standard deviation from three independent FTS runs. Dashed lines correspond to RPA Eq. 32. The reduced temperature,  $T_0^*$  (top horizontal scale), used in the analytical theories presented in this work is defined by  $T_0^* = l/l_B$ , where  $l = \sqrt{6}a$  is the reference polymer bond length of the polyampholyte chains<sup>53</sup> to be discussed below. The magnitude of the dipole moment,  $\mu$ , is in units of  $el$ .  $l$  is equivalent to the reference bond length  $a$  used in Eq. 12 for  $T_0^*$  in the molecular dynamics study.

**Analytical Theory for Mixture of Dipole and Nonpolar Solvents.** Before introducing polymers to the pure dipole systems described above, it is instructive to first consider the simpler case of an incompressible mixture of fixed dipoles and nonpolar (and nonpolarizable) particles as a model of nonpolar solvent molecules. For this purpose, we add  $n_n$  Gaussian-smearred particles with positions  $\mathbf{r}_{n,i}$  and modify the incompressibility condition

in Eq. 17 to

$$\rho_w(\mathbf{r}) + \rho_n(\mathbf{r}) = \frac{1}{v}, \quad (34)$$

where  $\rho_n(\mathbf{r}) = \sum_{i=1}^{n_n} \Gamma(\mathbf{r} - \mathbf{r}_{n,i})$ . The canonical partition function for this system is

$$\mathcal{Z} = \frac{1}{n_w!n_n!} \prod_{i=1}^{n_n} \int d\mathbf{r}_{n,i} \prod_{i=1}^{n_w} \int d\mathbf{r}_i \int d\boldsymbol{\mu}_i e^{-\mathcal{U}} \delta \left[ \rho_w(\mathbf{r}) + \rho_n(\mathbf{r}) - \frac{1}{v} \right], \quad (35)$$

where  $\mathcal{U}$  is unchanged. Accordingly, the field theory version of the partition function is given by

$$\mathcal{Z} = \frac{\Omega^{n_w+n_n}}{n_w!n_n!} \int \mathcal{D}w \int \mathcal{D}\psi e^{-\mathcal{H}}, \quad (36)$$

where now

$$\mathcal{H}[w, \psi] = -n_w \ln \mathcal{Q}_w - n_n \ln \mathcal{Q}_n + \frac{1}{2\Omega} \sum_{\mathbf{k} \neq \mathbf{0}} \frac{\mathbf{k}^2}{4\pi l_B} \hat{\psi}(\mathbf{k}) \hat{\psi}(-\mathbf{k}) - \frac{i}{v} \hat{w}(\mathbf{0}) \quad (37)$$

includes a term with the partition function  $\mathcal{Q}_n$  for a single nonpolar particle, viz.,

$$\mathcal{Q}_n = \frac{1}{\Omega} \int d\mathbf{r} \exp \left\{ -\frac{i}{\Omega} \sum_{\mathbf{k}} \hat{w}(\mathbf{k}) \hat{\Gamma}(-\mathbf{k}) e^{-i\mathbf{k} \cdot \mathbf{r}} \right\}. \quad (38)$$

With this setup, once again we can apply Eq. 28 to compute the bulk relative permittivity of mixtures of the two solvents, both in RPA and FTS. In RPA,

$$\epsilon_r = 1 + \chi_D \phi_w, \quad (39)$$

where  $\phi_w = vn_w/\Omega$  is the dipole volume fraction. The corresponding FTS calculation follows the same recipe as under the previous subheading, but now with the field Hamiltonian in Eq. 37. Comparisons between  $\epsilon_r$  computed in RPA and FTS are shown in Figs. 8 and 9 for  $\mu = 0.2$  and  $\mu = 0.35$ , respectively, for a wide range of  $l_B$  values. Common to all runs are the parameter values  $v = 0.1$  and  $\bar{a} = 1/\sqrt{6}$ . FTS follows RPA quite well except at high  $l_B$  and intermediate  $\phi_w$  where the FTS  $\epsilon_r$  can be substantially lower than the RPA  $\epsilon_r$  (see, e.g., Fig. 9c).

This drop in  $\epsilon_r$  may be understood by envisioning the system entering into an inhomogeneous state where a dipole-rich and a dipole-depleted phase coexist. Obviously, by construction, this phase separation is entirely driven by the electrostatic dipole-dipole interactions; and the system may be viewed as a special case of a binary mixture of two types of dipoles distinguished only by their dipole moments, which has been considered in ref. 95. In this reference, the virial expansion of such a system was studied using RPA, and

it was shown that there is an effective Flory  $\chi$  parameter, proportional to the square of the difference in dipole moment, that can induce phase separation. By directly calculating  $\mathcal{Z}$  in RPA, we can subsequently compute the binodal curve using the free energy  $f = -\ln \mathcal{Z} / \Omega$ . In RPA, the field Hamiltonian still follows Eq. 29, but now with

$$\hat{\Delta}_k = \begin{pmatrix} \hat{\Gamma}_k^2/v & 0 \\ 0 & (k^2/4\pi l_B) \left(1 + \chi_D \hat{\Gamma}_k^2 \phi_w\right) \end{pmatrix}, \quad (40)$$

which leads to the free energy

$$f = \phi_w \ln \phi_w + (1 - \phi_w) \ln(1 - \phi_w) + \frac{v}{4\pi^2} \int_0^\infty dk k^2 \ln \left[1 + \chi_D \phi_w \hat{\Gamma}^2\right] \quad (41)$$

up to an additive constant. Fig. 10 shows the phase diagram computed for the two values of the dipole moment in Figs. 8 and 9 using this free energy. Dotted horizontal lines indicate the  $l_B$  values considered in FTS. Indeed, we see that the parameter values for which FTS and RPA do not quite agree with regard to  $\epsilon_r$  ( $l_B = 300$  for  $\mu = 0.2$  in Fig. 8 and  $l_B = 150$  for  $\mu = 0.35$  in Fig. 9) coincide well with parameter values in Fig. 10 for which RPA predicts phase separation with significant differences in dilute- and condensed-phase  $\phi_w$ s.

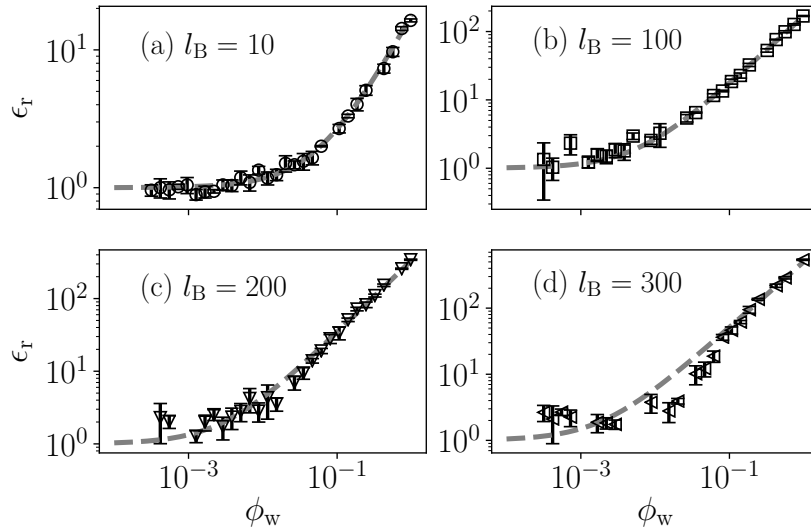


**Fig. 8:** Relative permittivity  $\epsilon_r$  computed in FTS and RPA for an incompressible mixture of fixed dipoles and nonpolar particles with  $\mu = 0.2$  at several values of  $l_B$  (in units of  $l$ ). As in Fig. 7, error bars are standard deviations of independent FTS runs, and dashed curves are RPA predictions.

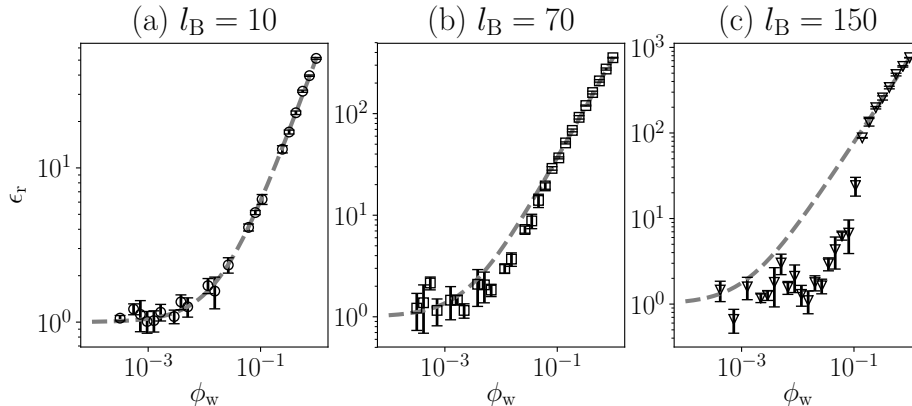


**Fig. 9:** Same as Fig. 8 but for  $\mu = 0.35$ .

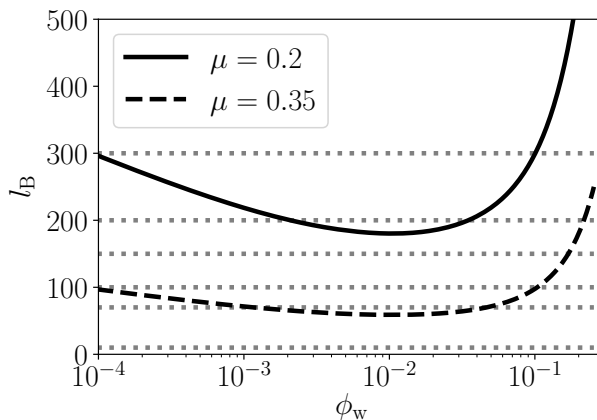


**Fig. 10:** Phase diagrams computed in RPA for incompressible mixtures of fixed dipoles and nonpolar particles. The binodal (coexistence) curves are shown for two values of the dipole moment,  $\mu = 0.2$  and  $\mu = 0.35$ ,  $v = 0.1$ , and  $\bar{a} = 1/\sqrt{6}$  (length unit =  $l$ , as noted for Fig. 7). The dashed horizontal lines indicate  $l_B$  values considered in FTS.

**Analytical Theory for Polyampholytes in Dipole Solvent.** We now consider systems consisting of  $n_w$  dipoles and, instead of nonpolar particles,  $n_p$  polyampholytes. Following the notation in ref. 53, each polyampholyte (labeled by  $\alpha$ ) is made up of  $N$  monomer beads (as in the above molecular dynamics simulations) at positions  $\mathbf{R}_{\alpha,\tau}$ ,  $\tau = 1, 2, \dots, N$ , and carries charge sequence  $|\sigma\rangle = [\sigma_1, \sigma_2, \dots, \sigma_N]^T$ . The incompressibility constraint for this system is given by

$$\rho_p(\mathbf{r}) + \rho_w(\mathbf{r}) = \frac{1}{v} \quad (42)$$

wherein the polymer matter (mass) density  $\rho_p(\mathbf{r}) = \sum_{\alpha=1}^{n_p} \sum_{\tau=1}^N \Gamma(\mathbf{r} - \mathbf{R}_{\alpha,\tau})$ . The Fourier-

transformed density of polymer charges,

$$\hat{c}(\mathbf{k}) = \hat{\Gamma}(\mathbf{k}) \sum_{\alpha=1}^{n_p} \sum_{\tau=1}^N \sigma_{\tau} e^{i\mathbf{k} \cdot \mathbf{R}_{\alpha, \tau}}, \quad (43)$$

now contribute to the Fourier-transformed total charge density such that

$$\hat{\rho}_c(\mathbf{k}) = \hat{c}(\mathbf{k}) + i\mathbf{k} \cdot \hat{\mathbf{m}}(\mathbf{k}). \quad (44)$$

The partition function of the polyampholytes-plus-dipoles system is given by

$$\mathcal{Z} = \frac{1}{n_p! n_w!} \prod_{\alpha=1}^{n_p} \prod_{\tau=1}^N \int d\mathbf{R}_{\alpha, \tau} \prod_{i=1}^{n_w} \int d\mathbf{r}_i \int d\boldsymbol{\mu}_i e^{-\mathcal{T}[\mathbf{R}] - \mathcal{U}[\mathbf{R}, \mathbf{r}]} \delta \left[ \rho_w(\mathbf{r}) + \rho_p(\mathbf{r}) - \frac{1}{v} \right], \quad (45)$$

where

$$\mathcal{T}[\mathbf{R}] = \frac{3}{2l^2} \sum_{\alpha=1}^{n_p} \sum_{\tau=1}^{N-1} (\mathbf{R}_{\alpha, \tau+1} - \mathbf{R}_{\alpha, \tau})^2 \quad (46)$$

is the Hamiltonian term for Gaussian chain connectivity,  $l$  is the reference bond length that we have used as a length scale in Fig. 7 to define  $T_0^*$  for the present analytical theories, and  $\mathcal{U}$  for electrostatic interactions takes the same general form as that given by Eq. 20. The field-theory expression for the partition in Eq. 45 is

$$\mathcal{Z} = \frac{\Omega^{n_p+n_w}}{n_p! n_w!} \int \mathcal{D}w \mathcal{D}\psi e^{-\mathcal{H}} \quad (47)$$

where

$$\mathcal{H}[\psi, w] = -n_p \ln \mathcal{Q}_p - n_w \ln \mathcal{Q}_w + \frac{1}{2\Omega} \sum_{\mathbf{k} \neq 0} \frac{\mathbf{k}^2}{4\pi l_B} \hat{\psi}(\mathbf{k}) \hat{\psi}(-\mathbf{k}) - \frac{i}{v} \hat{w}(\mathbf{0}) \quad (48)$$

and, via Hubbard-Stratonovich transformation, the single-polymer partition function  $\mathcal{Q}_p$  is given by

$$\mathcal{Q}_p = \frac{1}{\Omega} \prod_{\tau=1}^N \int d\mathbf{R}_{\tau} \exp \left\{ -\frac{3}{2l^2} \sum_{\tau=1}^{N-1} (\mathbf{R}_{\tau+1} - \mathbf{R}_{\tau})^2 - \frac{i}{\Omega} \sum_{\mathbf{k}} \sum_{\tau=1}^N [\hat{w}(\mathbf{k}) + \sigma_{\tau} \hat{\psi}(\mathbf{k})] \hat{\Gamma}(-\mathbf{k}) e^{-i\mathbf{k} \cdot \mathbf{R}_{\tau}} \right\}. \quad (49)$$

As in the above analysis of pure dipoles and dipoles-plus-nonpolar-particles systems, we may now expand the field Hamiltonian to second order in the fields to arrive at an RPA theory. Again, this leads to the general RPA form in Eq. 29, now with a different expression

for the kernel  $\hat{\Delta}_k$  for the system described by Eq. 45:

$$\hat{\Delta}_k = \begin{pmatrix} (\phi g_k^{\text{mm}} + \phi_w) \hat{\Gamma}_k^2 / v & \phi g_k^{\text{mc}} \hat{\Gamma}_k^2 / v \\ \phi g_k^{\text{mc}} \hat{\Gamma}_k^2 / v & (\phi g_k^{\text{cc}} + \mathcal{D} \phi_w k^2) \hat{\Gamma}_k^2 / v + (k^2 / 4\pi l_B) \end{pmatrix}, \quad (50)$$

where  $\mathcal{D} = \mu^2/3$  for intrinsic dipoles and  $\mathcal{D} = 1/(\beta\kappa_d)$  for induced (polarizable) dipoles. Here  $\phi = vNn_p/\Omega$  is the polymer volume fraction (thus  $\phi_w = 1 - \phi$  is the dipole volume fraction). The factors  $g_k^{\text{mm}}$ ,  $g_k^{\text{mc}}$  and  $g_k^{\text{cc}}$  stem from the single-polymer partition function in Eq. 49,

$$g_k^{\text{mm}} = \frac{1}{N} \sum_{\nu, \tau=1}^N \exp(-l^2 k^2 |\nu - \tau| / 6), \quad (51a)$$

$$g_k^{\text{mc}} = \frac{1}{N} \sum_{\nu, \tau=1}^N \sigma_\nu \exp(-l^2 k^2 |\nu - \tau| / 6), \quad (51b)$$

$$g_k^{\text{cc}} = \frac{1}{N} \sum_{\nu, \tau=1}^N \sigma_\nu \sigma_\tau \exp(-l^2 k^2 |\nu - \tau| / 6). \quad (51c)$$

Applying the RPA form of the Hamiltonian  $\mathcal{H}$  in Eq. 29 to the expression for  $\mathcal{Z}$  in Eq. 22 and performing the  $\int \mathcal{D}w \mathcal{D}\psi$  integrals by including the prefactors of  $\int d\hat{w}(\mathbf{k}) \int d\hat{\psi}(\mathbf{k})$  in Eq. 24 lead to the following expression for the free energy  $f = -\ln \mathcal{Z} / \Omega$  in RPA:

$$f = \frac{\phi}{N} \ln \phi + (1 - \phi) \ln(1 - \phi) + \frac{v}{4\pi^2} \int_0^\infty dk k^2 \ln \left[ \frac{4\pi l_B v}{k^2} \det \hat{\Delta}_k \right], \quad (52)$$

where  $\hat{\Delta}_k$  is here given by Eq. 50. We rewrite the argument of the logarithm in the above integrand in the form of

$$\frac{(4\pi l_B v / k^2) \det \hat{\Delta}_k}{(4\pi l_B v / k^2) \det \hat{\Delta}_k \Big|_{\phi=0}} = 1 + \mathcal{A}_k \phi + \mathcal{B}_k \phi^2 \quad (53)$$

to arrive at a form of  $f$  in which irrelevant constant terms are subtracted, with

$$\mathcal{A}_k = g_k^{\text{mm}} - 1 + \frac{4\pi l_B}{vk^2(1 + \chi_D \hat{\Gamma}_k^2)} \hat{\Gamma}_k^2 (g_k^{\text{cc}} - k^2 \mathcal{D}), \quad (54a)$$

$$\mathcal{B}_k = \frac{4\pi l_B}{vk^2(1 + \chi_D \hat{\Gamma}_k^2)} \hat{\Gamma}_k^2 [(g_k^{\text{mm}} - 1)(g_k^{\text{cc}} - k^2 \mathcal{D}) - (g_k^{\text{mc}})^2]. \quad (54b)$$

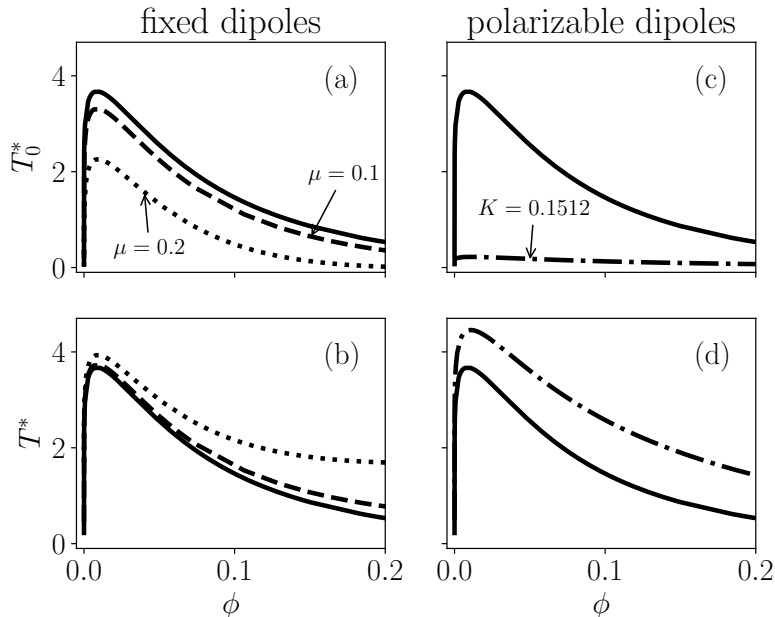


**Fig. 11:** RPA phase diagrams of incompressible mixtures of polyampholytes and dipoles. Results are for sequence sv15 with  $v = 0.1$  and  $\bar{a} = 1/\sqrt{6}$  (length unit =  $l$ ).  $\phi$  is polymer volume fraction,  $T_0^* = l/l_B$  is vacuum reduced temperature as in Fig. 7, and  $T^* = T_0^* \epsilon_r(\phi = 0)$  is reduced temperature that takes into account bulk-solvent relative permittivity (which is temperature dependent for fixed dipoles). Several solvent models are compared. Solid curves (all panels) are for nonpolar solvent ( $\mu = 0$ ); dashed and dotted curves [(a) and (b)] are for fixed-dipole solvents with  $\mu = 0.2$  and  $\mu = 0.1$ , respectively; and dashed-dotted curves [(c) and (d)] are for polarizable-dipole solvent with  $K = 0.1512$  (which, according to Eq. 32, entails a temperature-independent bulk-solvent  $\epsilon_r(\phi = 0) = 20$ ). Note that the  $l_B$  values considered in this figure are much lower than that required for the dipoles to phase separate on their own (Figs. 8–10).

At this juncture, we are in a position to use Eq. 52 to compute phase diagrams in RPA. Fig. 11 shows such phase diagrams in the  $(\phi, T_0^*)$  plane for polyampholyte chains with charge sequence sv15 immersed in fixed dipoles (Fig. 11a) and polarizable dipoles (Fig. 11c). Not surprisingly, compared to the case with nonpolar solvent (solid curves), LLPS propensity is lowered in the presence of polar solvents (dashed, dotted, and dashed-dotted curves in Figs. 11a and c) because the LLPS-driving effective electrostatic interactions among the polyampholytes are weakened due to screening, and this LLPS-suppressing effect increases with increasing polarity of the solvent ( $T_{0,cr}^*$  lower for  $\mu = 0.2$  than for  $\mu = 0.1$  in Fig. 11a). This comparison corresponds to that between models (i) and (ii) in Fig. 6a for the corresponding molecular dynamics results. Figs. 11b and d show the corresponding phase diagrams in the  $(\phi, T^*)$  plane, where  $T^* = T_0^* \epsilon_r(\phi = 0)$  with  $\epsilon_r(\phi = 0)$  being the relative permittivity of the bulk-solvent. These plots offer a comparison between the phase behavior of polyampholytes interacting via a homogeneous background dielectric constant (solid curves) and the phase behavior of polyampholytes interacting with an incompressible

dipole solvent (thus allowing for dipole-concentration-dependent relative permittivity) with the same bulk-solvent relative permittivity. Thus this comparison corresponds to that between molecular dynamics models (iii) and (ii) in Fig. 6a. Interestingly, whereas models (iii) and (ii) for sv15 in Fig. 6a exhibit essentially the same LLPS propensity—a feature that may be caused by the relative weak electrostatic interactions in sv15 being largely overwhelmed by the attractive LJ interactions, RPA predictions in Figs. 11b and d indicate that interacting with an incompressible dipole solvent enhances polyampholyte LLPS propensity relative to that predicted for the corresponding situation with a homogeneous background dielectric constant. This enhancing effect is quite small for the fixed dipoles in Fig. 11b—the effect nonetheless increases with  $\mu$ —but the effect is more appreciable for the case of polarizable dipoles in Fig. 11d. As discussed previously,<sup>57</sup> because there are relatively strong non-electrostatic background attractive LJ interactions in the molecular dynamics model—interactions that are absent in the present theoretical formulation, the upward concavity on the condensed sides of the RPA coexistence curves in Fig. 11 is not observed for the molecular dynamics coexistence curves in Fig. 6.

**Comparison of Theory-Predicted Polyampholyte Phase Behaviors Under Different Relative Permittivity Models.** To clarify the difference between various permittivity models that have been employed by our group to study polyampholyte LLPS using analytical theories,<sup>29,35,51</sup> we take the mean-field limit for mass-density fluctuation, i.e.  $w \rightarrow 0$ , of the above formulation to focus on features of the RPA electrostatic free energy. In such a limit, only the bottom-right component of the  $\hat{\Delta}$  array in Eq. 50 remains, viz.

$$\hat{\Delta}_k \xrightarrow{w \rightarrow 0} \frac{1}{v} [\phi g_k^{cc} + (1 - \phi) \mathcal{D}k^2] \hat{\Gamma}_k^2 + \frac{k^2}{4\pi l_B}. \quad (55)$$

The RPA electrostatic free energy is then given by

$$f_{\text{el}} = \frac{v}{4\pi^2} \int_0^\infty dk k^2 \ln \left[ 1 + \chi_D \hat{\Gamma}_k^2 (1 - \phi) + \frac{4\pi l_B}{vk^2} g_k^{cc} \hat{\Gamma}_k^2 \phi \right], \quad (56)$$

which may be rewritten as

$$\begin{aligned} f_{\text{el}} &= \frac{v}{4\pi^2} \int_0^\infty dk k^2 \ln \left[ 1 + \chi_D \hat{\Gamma}_k^2 (1 - \phi) \right] + \frac{v}{4\pi^2} \int_0^\infty dk k^2 \ln \left[ 1 + \frac{4\pi l_B g_k^{cc} \hat{\Gamma}_k^2 \phi}{vk^2 [1 + \chi_D \hat{\Gamma}_k^2 (1 - \phi)]} \right] \\ &\equiv f_{\text{el}}^{\text{dd}} + f'_{\text{el}} \end{aligned} \quad (57)$$

in which the first term  $f_{\text{el}}^{\text{dd}}$  accounts for dipole-dipole interaction between solvent molecules, and the second term includes charge-charge (polymer-polymer) and charge-dipole (polymer-solvent) interactions. It should be noted that in the present system, the pure material sus-

ceptibilities are  $\chi_D^p = 0$  for polymers (polyampholytes) and  $\chi_D^w = \chi_D$  for solvent molecules (dipoles). A concentration-dependent permittivity which for analytical tractability is assumed to be dependent linearly on volume fractions<sup>35</sup> can then be constructed as

$$\begin{aligned}
 \epsilon_r(\phi) &= \epsilon_p \phi + \epsilon_w (1 - \phi) \\
 &= (1 + \chi_D^p) \phi + (1 + \chi_D^w)(1 - \phi) \\
 &= \phi + (1 + \chi_D)(1 - \phi) \\
 &= 1 + \chi_D(1 - \phi).
 \end{aligned} \tag{58}$$

Thus, in the case of vanishing Gaussian smearing, i.e.  $\bar{a} \rightarrow 0$  and  $\Gamma_k \rightarrow 1$ , the second term in Eq. 57 can be cast in the following form:

$$\lim_{\hat{\Gamma}_k \rightarrow 1} f'_{\text{el}} = f_{\text{el}}^{\text{emp}} = \frac{v}{4\pi^2} \int_0^\infty dk k^2 \ln \left[ 1 + \frac{4\pi l_B}{v\epsilon_r(\phi)k^2} g_k^{\text{cc}} \phi \right], \tag{59}$$

where the superscript ‘‘emp’’ stands for ‘‘empirical permittivity’’. It is noteworthy that  $f_{\text{el}}^{\text{emp}}$  derived above is equivalent to the RPA electrostatic energy of the recent ‘‘with ‘self-energy’’ model used in Fig. 7B of Das et al.<sup>35</sup> More specifically, with  $v = l^3$ ,  $f_{\text{el}}^{\text{emp}}$  is seen to be identical to the expression in Eq. S60 in the SI Appendix of ref. 35, which in turn is based on the partition function  $\mathcal{Z}_{\text{el}}$  in Eq. S51 of the same reference.

We now proceed to clarify how dipole-dipole interactions promote LLPS whereas dipole-polymer interactions mostly suppress LLPS in the present analytical models. First, a small- $\phi$  Taylor expansion of the logarithmic integrand of  $f_{\text{el}}^{\text{dd}}$  in Eq. 57 yields

$$\ln \left[ 1 + \chi_D \hat{\Gamma}_k^2 (1 - \phi) \right] = \ln \left[ 1 + \chi_D \hat{\Gamma}_k^2 \right] - \frac{\chi_D \hat{\Gamma}_k^2}{1 + \chi_D \hat{\Gamma}_k^2} \phi - \frac{1}{2} \left( \frac{\chi_D \hat{\Gamma}_k^2}{1 + \chi_D \hat{\Gamma}_k^2} \right)^2 \phi^2 + \mathcal{O}(\phi^3), \tag{60}$$

wherein  $\phi^2$  is seen to associate with a negative factor, indicating that dipole-dipole interactions contribute an effectively attractive polymer-polymer interaction. In other words, dipole-dipole interactions contribute a positive Flory-Huggins  $\chi$  parameter or a negative second virial coefficient and therefore promote polymer phase separation. It should be noted as well that an equivalent conclusion can be reached by considering a Taylor expansion with respect to the mean-field concentration of the solvent molecules,  $(1 - \phi)$ , leading to the conclusion that the effective interactions among the dipoles are also attractive.

Second, we note that the  $f'_{\text{el}}$  term in Eq. 57 for the ‘‘empirical permittivity’’ model may

be dissected further by rewriting it in the following form:

$$f'_{\text{el}} = \frac{v}{4\pi^2} \int_0^\infty dk k^2 \ln \left[ 1 + \frac{4\pi l_{\text{B}}}{vk^2} g_k^{\text{cc}} \hat{\Gamma}_k^2 \phi \right] + \frac{v}{4\pi^2} \int_0^\infty dk k^2 \ln \left[ 1 - \frac{\frac{4\pi l_{\text{B}}}{vk^2} \left( \frac{\bar{\chi}_{\text{D}}}{1+\bar{\chi}_{\text{D}}} \right) g_k^{\text{cc}} \hat{\Gamma}_k^2 \phi}{1 + \frac{4\pi l_{\text{B}}}{vk^2} g_k^{\text{cc}} \hat{\Gamma}_k^2 \phi} \right]. \quad (61)$$

Here the first term is the RPA theory with constant vacuum permittivity, i.e. purely charge-charge (polymer-polymer) interactions, and the second term accounts for charge-dipole (polymer-solvent) interactions, and we have defined  $\bar{\chi}_{\text{D}} \equiv \chi_{\text{D}} \Gamma_k^2 (1 - \phi)$ . A Taylor expansion of the second term with respect to  $\phi$  gives

$$\ln \left[ 1 - \frac{\frac{4\pi l_{\text{B}}}{vk^2} \left( \frac{\bar{\chi}_{\text{D}}}{1+\bar{\chi}_{\text{D}}} \right) g_k^{\text{cc}} \hat{\Gamma}_k^2 \phi}{1 + \frac{4\pi l_{\text{B}}}{vk^2} g_k^{\text{cc}} \hat{\Gamma}_k^2 \phi} \right] = -\frac{A_k B_k}{B_k + 1} \phi + \frac{A_k B_k (A_k B_k + 2A_k + 2)}{2(B_k + 1)^2} \phi^2 + \mathcal{O}(\phi^3), \quad (62)$$

where

$$A_k \equiv \frac{4\pi l_{\text{B}}}{vk^2} g_k^{\text{cc}} \hat{\Gamma}_k^2, \quad B_k = \chi_{\text{D}} \hat{\Gamma}_k^2. \quad (63)$$

Given  $A_k, B_k > 0 \forall k$ , the polymer-dipole interactions entail a positive second virial coefficient associated with the  $\phi^2$  term in Eq. 62 that equals to

$$\frac{v}{4\pi^2} \int_0^\infty dk k^2 \frac{A_k B_k (A_k B_k + 2A_k + 2)}{2(B_k + 1)^2} > 0, \quad (64)$$

which acts as an effective excluded-volume-like repulsion between polymers and thus suppress phase separation.

The comparison above is between two models with the same polymer relative permittivity ( $\epsilon_{\text{p}} = 1$ ) but different solvent relative permittivities ( $\epsilon_{\text{w}} = 1$  versus  $\epsilon_{\text{w}} = 1 + \chi_{\text{D}}$ , see Eq. 58). Another comparison, of more direct interest to the question at hand, is between an implicit-solvent model in which the polymers interact in a dielectric environment with a constant  $\epsilon_{\text{w}} = 1 + \chi_{\text{D}}$  (the relative permittivity of the polymer material itself remains the same at  $\epsilon_{\text{p}} = 1$ ) and the full theory with the polymers immersed in dipole solvent wherein the bulk-dipole relative permittivity is  $\epsilon_{\text{w}} = 1 + \chi_{\text{D}}$ . This comparison may be analyzed by using a modified Bjerrum length,  $l_{\text{B}}^{\text{r}} = l_{\text{B}}/\epsilon_{\text{w}}$ , as characteristic temperature factor, to regroup Eq. 61 for  $f'_{\text{el}}$  into a sum of two contributions,

$$f'_{\text{el}} = \frac{v}{4\pi^2} \int_0^\infty dk k^2 \ln \left[ 1 + \frac{4\pi l_{\text{B}}^{\text{r}}}{vk^2} g_k^{\text{cc}} \hat{\Gamma}_k^2 \phi \right] + \frac{v}{4\pi^2} \int_0^\infty dk k^2 \ln \left[ 1 + \frac{\frac{4\pi l_{\text{B}}^{\text{r}}}{vk^2} g_k^{\text{cc}} \hat{\Gamma}_k^2 \left( \frac{1+\chi_{\text{D}}}{1+\bar{\chi}_{\text{D}}} - 1 \right) \phi}{1 + \frac{4\pi l_{\text{B}}^{\text{r}}}{vk^2} g_k^{\text{cc}} \hat{\Gamma}_k^2 \phi} \right], \quad (65)$$

such that the first term is the electrostatic free energy for polymers interacting with a constant implicit-solvent  $\epsilon_{\text{w}} = 1 + \chi_{\text{D}}$ . The integrand of the second term in Eq. 65, which

is a polymer-solvent interaction term, can now be expanded with respect to  $\phi$ :

$$\begin{aligned} \ln \left[ 1 + \frac{\frac{4\pi l_B^r}{vk^2} g_k^{cc} \hat{\Gamma}_k^2 \left( \frac{1+\chi_D}{1+\bar{\chi}_D} - 1 \right) \phi}{1 + \frac{4\pi l_B^r}{vk^2} g_k^{cc} \hat{\Gamma}_k^2 \phi} \right] &= - \frac{A_k^r \chi_D (\hat{\Gamma}_k^2 - 1)}{\chi_D \hat{\Gamma}_k^2 + 1} \phi \\ &+ \frac{A_k^r \chi_D \left\{ A_k^r (\hat{\Gamma}_k^2 - 1) \left[ \chi_D (\hat{\Gamma}_k^2 + 1) + 2 \right] + 2(1 + \chi_D) \hat{\Gamma}_k^2 \right\}}{2 \left( \chi_D \hat{\Gamma}_k^2 + 1 \right)^2} \phi^2 \\ &+ \mathcal{O}(\phi^3), \end{aligned} \quad (66)$$

where  $A_k^r = 4\pi l_B^r / (vk^2) g_k^{cc} \hat{\Gamma}_k^2$ . Now, the form of the the second virial coefficient, denoted  $v_2^{\text{pw},r}$ , that associates with the  $\phi^2$  term,

$$v_2^{\text{pw},r} = \frac{v}{4\pi^2} \int_0^\infty dk k^2 \frac{A_k^r \chi_D \left\{ A_k^r (\hat{\Gamma}_k^2 - 1) \left[ \chi_D (\hat{\Gamma}_k^2 + 1) + 2 \right] + 2(1 + \chi_D) \hat{\Gamma}_k^2 \right\}}{2 \left( \chi_D \hat{\Gamma}_k^2 + 1 \right)^2}, \quad (67)$$

becomes rather intricate. To analyze the sign of  $v_2^{\text{pw},r}$ , we substitute the definition of  $A_k^r$  into the numerator of the integrand in the above expression and rewrite it as

$$\frac{4\pi l_B^r \chi_D}{v} \frac{g_k^{cc}}{k^2} \hat{\Gamma}_k^4 \left[ \frac{4\pi l_B^r}{vk^2} g_k^{cc} \left( \hat{\Gamma}_k^2 - 1 \right) \left( \chi_D \hat{\Gamma}_k^2 + \chi_D + 2 \right) + 2(1 + \chi_D) \right]. \quad (68)$$

For overall neutral polyampholytes,  $g_k^{cc} \ll 1$  when  $k \rightarrow 0$ ,  $g_k^{cc} \rightarrow 1$  when  $k \rightarrow \infty$ , and  $g_k^{cc}$  does not increase monotonically with  $k$  but has a peak at some intermediate  $k$  for most cases (except, e.g., for the strictly alternating sequence sv1, which monotonically increases from 0 to 1 when  $k$  increases). For  $k \ll 1/\bar{a}$ ,  $\hat{\Gamma}_k \rightarrow 1$ , the general expression in Eq. 68 becomes

$$\frac{8\pi l_B^r \chi_D (1 + \chi_D)}{v} \frac{g_k^{cc}}{k^2} \left[ - \frac{4\pi l_B^r \bar{a}^2}{v} g_k^{cc} + 1 \right] > 0, \quad (69)$$

and for  $k \gg 1/\bar{a}$ ,  $\hat{\Gamma}_k \rightarrow 0$ , the same general expression becomes

$$\frac{8\pi l_B^r \chi_D (1 + \chi_D)}{v} \frac{g_k^{cc}}{k^2} \hat{\Gamma}_k^4 > 0. \quad (70)$$

Thus, Eq. 68 contributes a repulsive effect to the integral for  $v_2^{\text{pw},r}$  in Eq. 67 in both the small- $k$  and large- $k$  regimes. Moreover, the  $\hat{\Gamma}_k^4$  factor in the same expression tends to reduce large- $k$  contributions to the  $v_2^{\text{pw},r}$  integral. Therefore, it is expected that as long as the peak of  $g_k^{cc}$  is at  $k \lesssim 1/\bar{a}$ , effective polymer-solvent interactions should be repulsive. However, in view of the intricate form of  $v_2^{\text{pw},r}$  in Eq. 67, the possibility of effective polymer-solvent interactions being attractive in certain extreme scenarios cannot be precluded.

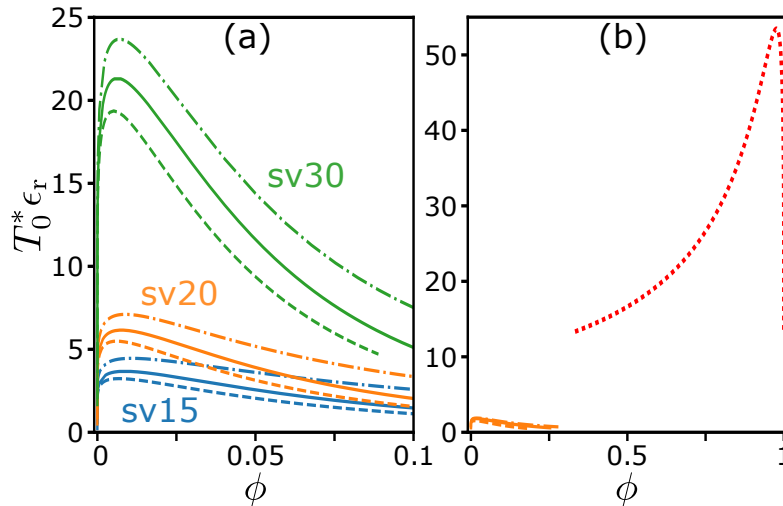


**Fig. 12:** Comparing RPA LLPS theories with different solvent permittivity models. The vertical variable  $T_0^* \epsilon_r = T^*$ , where  $\epsilon_r$  is bulk-solvent relative permittivity. (a) Coexistence curves of sequences sv15, sv20, and sv30 are shown in different colors. Dashed-dotted curves are for the full explicit dipole solvent model, solid curves are for the implicit-solvent constant permittivity model (with nonpolar solvent). Both set of curves are computed with the mass density conjugate field  $w$  in accordance with the formulation given by Eqs. 52–54 (dashed-dotted and solid curves for sv15 are the same as those in Fig. 11d). Dashed curves are for the empirical permittivity model, computed in the  $w \rightarrow 0$  formulation wherein excluded volume is implemented by incompressibility at the mean-field level (electrostatic free energy given by the second term in Eq. 57). All coexistence curves in (a) are computed using  $v = 0.1$  (in units of  $l^3$ ). (b) Coexistence curves for sv20 with the same models in (a) depicted in the same line styles in orange but all computed using the  $w \rightarrow 0$  formulation with  $v = 1.0$  (Eq. 56 with  $l_B \rightarrow l_B^e = l_B/\epsilon_w$  for dashed-dotted curve, first term in Eq. 65 for solid curve, and second term in Eq. 57, as in (a), for dashed curve). The red dotted curve for a “no self energy” model is the coexistence curve computed using an electrostatic free energy equals to that of the empirical permittivity model (second term in Eq. 57) minus the “self-energy” term in Eq. 71.

Fig. 12a compares the theory-predicted phase behaviors of sequences sv15, sv20, and sv30 under three different relative permittivity models for the solvent. All three sequences studied exhibit the same ranking ordering of LLPS propensities for the three models (as quantified by their critical temperatures):

$$\text{explicit dipole solvent} > \text{constant permittivity} > \text{empirical permittivity} .$$

While recognizing that two of the solvent models investigated in Fig. 12a use the theoretical formulation with the matter conjugate field  $w$  (Eqs. 52–54), it is noteworthy that the rank ordering of LLPS propensity in Fig. 12a is consistent with the above  $w \rightarrow 0$  analysis. First, because dipole-dipole interactions in the explicit dipole solvent model enhance phase separation,

ration relative to the empirical model (Eqs. 57 and 60), explicit dipole solvent  $>$  empirical permittivity. Second, after subtracting the free energy for the constant permittivity model from the free energy  $f'_{\text{el}}$  for the empirical permittivity model, a LLPS-disfavoring repulsive term probably remains (Eqs. 65, 67–70 and discussion that follows), i.e., it is likely that constant permittivity  $>$  empirical permittivity. These analytical trends thus provide a partial rationalization of the rank ordering of LLPS propensity in Fig. 12a, although the above  $w \rightarrow 0$  consideration does not address the relative LLPS propensities of explicit dipole solvent and constant permittivity models.

In previous RPA studies of LLPS by our group, a “self-energy” term was subtracted from the RPA electrostatic free energy for calculational convenience.<sup>29,51</sup> While the procedure is valid for polyampholytes interacting in a medium of uniform relative permittivity because in that case the self-energy term does not affect phase behaviors,<sup>29</sup> the procedure is problematic for systems with polymer-concentration-dependent relative permittivity because in those situations the self-energy term may capture part of the polymer-solvent interactions and therefore can impact phase equilibrium, as we have pointed out recently.<sup>35</sup> The present analysis allows for further evaluation of such a self-energy term. Consider, in the theoretical framework developed above, the expression

$$f_{\text{self}} \equiv \int_0^\infty \frac{dk k^2}{4\pi^2} \frac{4\pi l_B}{\epsilon_r(\phi) k^2 N} \hat{\Gamma}_k^2 \phi \sum_{\tau=1}^N \sigma_\tau^2, \quad (71)$$

which can be seen to be equivalent to the self-energy  $\mathcal{G}_2(\tilde{k})$  quantity in Eq. 69b of ref. 29 when there is no salt or counterion ( $\phi_s = \phi_c = 0$ ), no short-range cutoff of Coulomb interactions ( $\tilde{k}^2[1 + \tilde{k}^2] \rightarrow k^2$ ), and  $\eta = 1$ , by noting that  $k = \tilde{k}/l$  ( $l$  now corresponds to  $b = a$  in ref. 29),  $l_B = l/T_0^*$ ,  $\hat{\Gamma}_k \rightarrow 1$  for  $\bar{a} \rightarrow 0$ , and that  $\sigma_i^2 = |\sigma_i|$  for polyampholytes with  $\sigma_i = \pm 1$ . An expansion of the factor  $[\epsilon_r(\phi)]^{-1} = [1 + \chi_D(1 - \phi)]^{-1}$  (Eq. 58) in the integrand for  $f_{\text{self}}$  in Eq. 71 yields

$$f_{\text{self}} = \int_0^\infty \frac{dk k^2}{4\pi^2} \frac{4\pi l_B}{k^2 N} \hat{\Gamma}_k^2 \phi \sum_{\tau=1}^N \sigma_\tau^2 [1 - \chi_D(1 - \phi) + \mathcal{O}(\chi_D^2)]. \quad (72)$$

This form conveys two messages. First, while a part of  $f_{\text{self}}$  may be identified with a part of  $f'_{\text{el}}$ , e.g., the term linear in  $\phi$  in the expansion of  $f_{\text{self}}$  is equal to a part of the first term (linear in  $\phi$ ) in the expansion of the logarithmic integrand of the first integral in Eq. 61 (the  $\mu = \nu$  part of the summation for  $g_k^{\text{cc}}$  in Eq. 51c), and therefore may be viewed as capturing part of polymer-solvent interactions,  $f_{\text{self}}$  by itself does not coincide with the free energy arising from polymer-solvent interactions. Second, the  $\phi^2$  term in the  $f_{\text{self}}$  expansion in Eq. 72 is positive, indicating that  $f_{\text{self}}$  entails an effective polymer-polymer repulsion. It follows that subtracting  $f_{\text{self}}$  should increase LLPS propensity. This effect

is illustrated by the coexistence curve in Fig. 12b computed using a free energy with  $f_{\text{self}}$  subtracted (dotted red curve). The dramatic increase in LLPS propensity of this model compared with corresponding models without the self-energy subtraction (orange curves) is in line with some of our previous results on models with self-energy subtraction (Fig. 12 of ref. 29). However, for other heteropolymer models with less charge densities and augmented Flory-Huggins interactions, subtracting an electrostatic self-energy term can lead to more modest—though still substantial—increases in LLPS propensity (Fig. 7C of ref. 35). Most importantly, the present analysis shows that a self-energy term similar to the one in Eq. 71 does not account neatly for polymer-solvent interactions, and in any event, subtraction of such a term from the RPA electrostatic free energy is physically unwarranted.

## DISCUSSION

**FTS of Polyampholytes with Dipole Solvent.** In addition to RPA, we have extended our FTS effort beyond the study of pure dipoles and dipole and nonpolar solvent mixtures (Figs. 7–9) to the investigation of polyampholyte LLPS in the presence of dipoles. In this endeavor, we find that the strict incompressibility constraint considered above for RPA (Eq. 42) is challenging to realize numerically in the fully fluctuating FTS simulations of systems comprised of polyampholytes and explicit polar solvents. Therefore, we opt instead for a compressible model in which the Dirac  $\delta[\rho_{\text{p}}(\mathbf{r}) + \rho_{\text{w}}(\mathbf{r}) - 1/v]$  for incompressibility is replaced by an energy penalty term in the interaction Hamiltonian in the form of  $\int d\mathbf{r}(\rho_{\text{p}}(\mathbf{r}) + \rho_{\text{w}}(\mathbf{r}) - 1/v)^2/2\gamma$ . The resulting system is incompressible in the  $\gamma \rightarrow 0$  limit but compressible for finite  $\gamma$ . The corresponding field-picture Hamiltonian is given by

$$\mathcal{H}[\psi, w] = \frac{1}{8\pi l_{\text{B}}} \int d\mathbf{r}(\nabla\psi(\mathbf{r}))^2 + \frac{\gamma}{2} \int d\mathbf{r}w(\mathbf{r})^2 - \frac{i}{v} \int d\mathbf{r}w(\mathbf{r}) - n_{\text{w}} \ln \mathcal{Q}_{\text{w}} - n_{\text{p}} \ln \mathcal{Q}_{\text{p}} , \quad (73)$$

where the partition functions  $\mathcal{Q}_{\text{w}}$  and  $\mathcal{Q}_{\text{p}}$  for a single dipole and a single polymer chain, respectively, are given by Eq. 25 and Eq. 49. We focus here on a solution comprised of a single species of polyampholytes and a single species of dipoles as a model of a polar solvent. The equilibrium averages of thermodynamic variables of the system are obtained by averaging over sufficiently large number of statistically independent configurations of the fields  $\psi$  and  $w$ . Following the CL prescription in Eq. 33, the field configurations are generated by numerically solving the following two coupled differential equations:

$$\begin{aligned} \frac{\partial w(\mathbf{r})}{\partial t} &= - \left[ i \left( \tilde{\rho}_{\text{p}}(\mathbf{r}) + \tilde{\rho}_{\text{w}}(\mathbf{r}) - \frac{1}{v} \right) + \gamma w(\mathbf{r}) \right] + \eta_w , \\ \frac{\partial \psi(\mathbf{r})}{\partial t} &= - \left[ i (\tilde{c}(\mathbf{r}) + \tilde{c}_{\text{w}}(\mathbf{r})) - \frac{1}{4\pi l_{\text{B}}} \nabla^2 \psi(\mathbf{r}) \right] + \eta_{\psi} . \end{aligned} \quad (74)$$

In Eq. 74,  $t$  is a fictitious time,  $\eta_w$  and  $\eta_\psi$  are real-valued random numbers drawn from a Normal distribution with zero mean and variance  $2\delta(t-t')\delta(\mathbf{r}-\mathbf{r}')$ , and the field operators for polymer bead density ( $\tilde{\rho}_p$ ), polymer charge density ( $\tilde{c}$ ), solvent bead density ( $\tilde{\rho}_w$ ) and solvent charge density ( $\tilde{c}_w$ ) are given by

$$\begin{aligned}\tilde{\rho}_p(\mathbf{r}) &= \frac{in_p}{\mathcal{Q}_p\Omega} \frac{\delta\mathcal{Q}_p}{\delta w}, & \tilde{c}(\mathbf{r}) &= \frac{in_p}{\mathcal{Q}_p\Omega} \frac{\delta\mathcal{Q}_p}{\delta\psi}, \\ \tilde{\rho}_w(\mathbf{r}) &= \frac{in_w}{\mathcal{Q}_w\Omega} \frac{\delta\mathcal{Q}_w}{\delta w}, & \tilde{c}_w(\mathbf{r}) &= \frac{in_w}{\mathcal{Q}_w\Omega} \frac{\delta\mathcal{Q}_w}{\delta\psi}.\end{aligned}\tag{75}$$

The individual solvent beads are overall charge neutral, but polar in nature with each having a fixed magnitude of dipole moment equals to  $\mu$ .  $\tilde{c}_w$  can be re-expressed by defining a solvent polarization density operator such that  $\tilde{c}_w = -\nabla \cdot \tilde{\mathbf{m}}(\mathbf{r})$  where

$$\tilde{\mathbf{m}}(\mathbf{r}) = \frac{in_w}{\mathcal{Q}_w\Omega} e^{-i\check{w}(\mathbf{r})} \frac{\nabla\check{\psi}(\mathbf{r})}{\left[\nabla\check{\psi}(\mathbf{r})\right]^2} \left[ \cos\left(\mu|\nabla\check{\psi}(\mathbf{r})|\right) - \frac{\sin\left(\mu|\nabla\check{\psi}(\mathbf{r})|\right)}{\mu|\nabla\check{\psi}(\mathbf{r})|} \right], \tag{76}$$

and the smeared fields in this expression, each marked by a diacritic breve, are defined by spatial convolution as  $\check{\varphi} = \Gamma \star \varphi$ ,  $\varphi = w, \psi$ . We integrate Eq. 74 numerically by using the first-order semi-implicit time integration method of ref. 125 over a cubic box of volume  $\Omega = (32\bar{a})^3$ . To achieve good numerical precision, we discretize the box into a  $32 \times 32 \times 32$  grid. The volume of a single bead is taken to be  $v = 0.1$ , the bulk polymer bead density is set at 0.47,  $\mu = 0.1$  and  $\gamma = 10$ . Although not rigorously identical to matter or charge densities, the CL time snapshots of density operators are an intuitive and instructive way to visualize phase separation in FTS systems.<sup>60,61,64</sup> Fig. 13 shows representative snapshots of the field operators of different observables for two different temperatures to illustrate that the present polyampholytes plus dipoles system can indeed undergo phase separation. As temperature is lowered from a relatively high temperature ( $T_0^* = 50$ ) to a relatively low temperature ( $T_0^* = 0.2$ ), polymer material (red) distributed rather uniformly throughout the simulation box at high temperature (Figs. 13d–f) is seen to coalesce into a droplet-like structure at low temperature (Figs. 13a–c). This FTS behavior is similar to that observed for molecular dynamics simulations in Fig. 5 for the same polyampholyte sequence sv20.

Technically, the cost of introducing compressibility is that we now have two independent chemical potentials corresponding to the polyampholytes and the solvent. This makes computation of thermodynamically consistent FTS phase diagrams difficult because the approach applied in refs. 60 and 127 is not workable for the present system and one needs to employ Gibbs ensemble FTS similar to methodologies used in refs. 61 and 128. Even so, the expected extreme dilute nature of the low-density phase in our FTS system of interest, as suggested by the RPA results in Figs. 11 and 12, would likely make it challenging to

arrive at a set of parameters for which the Gibbs ensemble FTS is numerically stable. Work is now underway to overcome these challenges.

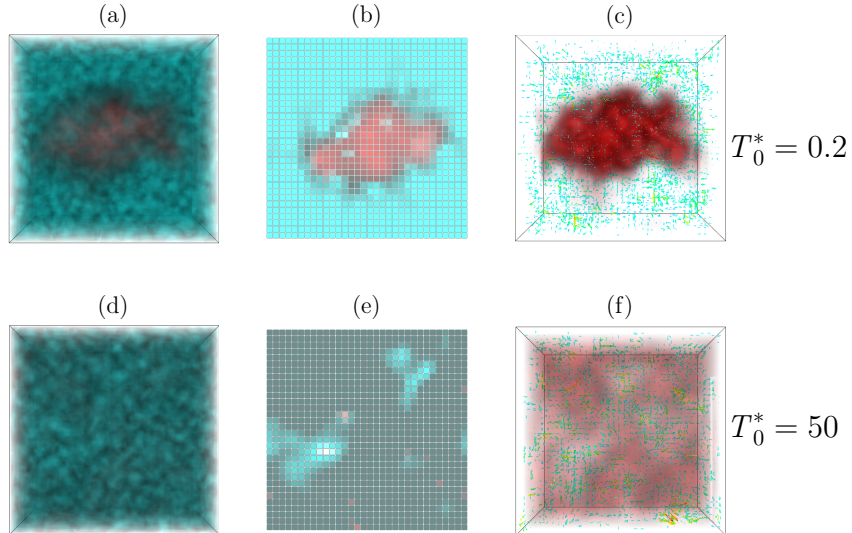


**Fig. 13:** Illustrative FTS snapshots of the density operators at low and high temperatures. All results shown are for polyampholyte sequence sv20, dipole  $\mu = 0.1$ , excluded-volume parameter  $v = 0.1$ , and  $\gamma = 10$ . (a) Temperature  $T_0^* = 0.2$ . Real non-zero parts of  $\tilde{\rho}_p(\mathbf{r})$  and  $\tilde{\rho}_w(\mathbf{r})$ . A droplet-like structure of sv20 molecules (shown in red) is buried inside the polar solvent (shown in cyan). (b) A cut-plane view of (a) of a thin slice of the simulation box parallel to the page. (c) sv20 droplet (in red) is depicted together with the real part of solvent (dipole) polarization operator  $\tilde{\mathbf{m}}(\mathbf{r})$  as arrows. (d)–(f): Same as (a)–(c), but at  $T_0^* = 50$ . Here, the polyampholytes and solvent are seen to distribute in an essentially uniform manner throughout the simulation box.

**The Distinctive Solvent Dielectric Environments in the Dilute and Condensed Phases Likely Contribute to a Minor Enhancement of Polyampholyte LLPS Propensity.** As reported above, our molecular dynamics and analytical RPA theories indicate, at least for the models considered, that allowing the solvent-contributed effective  $\epsilon_r$  inside a condensed polyampholyte-rich droplet to decrease by using a physically plausible explicit polar solvent model (Fig. 4) leads in most cases to an enhancement of polyampholyte LLPS propensity relative to that predicted by commonly utilized implicit-solvent formulations in which the polyampholytes interact electrostatically via  $\epsilon_r$  of the bulk solvent (Figs. 6, 11, and 12). However, contrary to earlier suggestions that this effect can be dramatic,<sup>29,51</sup> the enhancement effect observed here is only minor or at most moderate. We may quantify the enhancement effect by the ratio of the critical temperature of the explicit-solvent model to that of the implicit-bulk-solvent, constant  $\epsilon_r$  model, or the percentage increase of the former over the latter. For the molecular dynamics results in Fig. 6, this percentage increase in critical temperature,  $[T_{0,\text{cr}}^*(\text{ii}) - T_{0,\text{cr}}^*(\text{iii})]/T_{0,\text{cr}}^*(\text{iii})$ , obtained from the

$T_{0,\text{cr}}^*$  values in Table 1 is approximately  $-2\%$  for sequence sv15,  $5\%$  for sv20, and  $11\%$  for sv30. These changes are minor, but nonetheless exhibit an increasing trend with increasing blockiness of the sequence charge pattern as characterized by  $-\text{SCD}$ , from essentially no change in  $T_{0,\text{cr}}^*$  for sv15 ( $-\text{SCD} = 4.35$ ) to a minor increase of  $11\%$  for sv30 ( $-\text{SCD} = 27.8$ ). In this context, it is interesting to note that for sv30,  $T_{0,\text{cr}}^*$  of the explicit-solvent model (ii) is almost identical to that of the explicit nonpolar solvent model with  $\epsilon_r = 1$  (i), suggesting in this case a relatively strong enhancement of polyampholyte LLPS by the heterogeneous dielectric environment entailed by the explicit-solvent model.

The corresponding RPA results in Fig. 12a also show minor to at most moderate increases. The  $T_{0,\text{cr}}^*, \epsilon_r$  values for the explicit dipole, constant permittivity, and empirical permittivity models in Fig. 12a are, respectively, 4.46, 3.37, and 3.24 for sv15, 7.10, 6.16, and 5.49 for sv20, and 23.7, 21.3, and 19.4 for sv30. For these models, while the increase in  $T_{0,\text{cr}}^*, \epsilon_r$  of the explicit dipole model over that of the constant permittivity model (difference between the two  $T_{0,\text{cr}}^*, \epsilon_r$  values) tends to increase with  $-\text{SCD}$  (1.09 for sv15, 0.94 for sv20, and 2.40 for sv30), the percentage increase in  $T_{0,\text{cr}}^*$  decreases with  $-\text{SCD}$ : approximately  $32\%$  for sv15,  $15\%$  for sv20, and  $11\%$  for sv30. To what extent are these differences between the molecular dynamics and RPA models attributable to their different bulk-solvent  $\epsilon_r$  values (4.0 for molecular dynamics, 20.0 for RPA) and their substantially different condensed-phase polymer volume fractions (much lower for RPA than for molecular dynamics) remains to be investigated. These uncertainties notwithstanding, the results in Figs. 6, 11, and 12 suggest that when all interactions among polyampholytes and polar solvents are appropriately taken into account, the enhancement of polyampholyte LLPS by the concentration-dependent dielectric heterogeneity of the polar solvent is likely minor. At the very least, one can be certain that the physical effect is much more modest than when part of the solvent-polymer interactions are neglected as in the case of the unphysical “no self energy” model depicted by the dotted red curve in Fig. 12b.

**The Dielectric Environment Experienced by Client Molecules in a Condensed Polyampholyte Droplet Can be Complex.** We have focused so far on the  $\epsilon_r$  contributed by the polar solvent and its concentration dependence (Figs. 4, 8, and 9) in order to gauge the solvent’s role in the effective LLPS-driving electrostatic interactions among the polyampholytes. In these formulations, the charges on the polyampholytes are treated explicitly, not as a part of the solvent-contributed dielectric background.<sup>29,35,51</sup> Once the polyampholyte-rich droplet—as a model biomolecular condensate—is formed, however, the dielectric environment entailed by the droplet as a whole—including contributions from both the polar solvent and the polyampholyte chains—is of potential biophysical and biochemical interest because, among its many effects, it would affect how other molecules, sometimes referred to as clients, partition into and interact within the droplet.

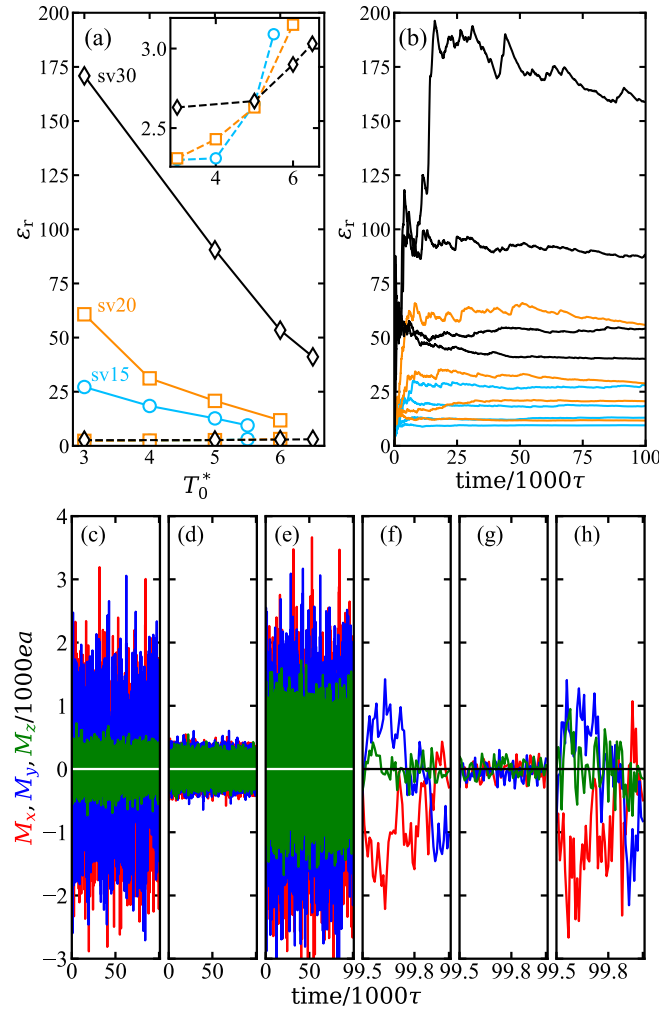


**Fig. 14:** Effective relative permittivity of condensed polyampholyte-rich droplets in dipole solvent computed by molecular dynamics simulations for the systems in Fig. 4. (a) For polyampholyte sequences sv15 (circles), sv20 (squares) and sv30 (diamonds), effective  $\epsilon_r$  inside each droplet (data points connected by solid lines) is obtained by applying Eq. 16 to local and global dipole moments contributed from both the polyampholytes and the dipole solvent molecules, wherein local dipole contributions are averaged over long simulation trajectories [shown in (b)] and averaged over the volume of the droplet delimited by an interval of width  $\Delta z$  in the  $z$ -direction of the simulation box. Included for comparison are effective  $\epsilon_r$  for each droplet contributed by the dipole solvent alone (data points connected by dashed lines at the bottom, shown also in the inset using a zoomed-in vertical scale for  $\epsilon_r$ ). The widths  $\Delta z/a$  of the droplets used for this calculation, listed by increasing temperature (same  $T_0^*$ s as those in Fig. 4), are: 40, 45, 60, 80 for sv15; 40, 45, 60, 85 for sv20; and 45, 60, 70, 80 for sv30. (b) Computed  $\epsilon_r$  as a function of sampling time for the systems in (a) using the same color code for the sequences, with  $T_0^*$  increasing from the bottom to top curve for each sequence. The time variable (horizontal axis) of Langevin molecular dynamics is in units of  $\tau$  (Models and Methods). (c)–(h) The variations of the  $x$ ,  $y$ , and  $z$  components of the dipole moment  $\mathbf{M}$ ,  $M_x$ ,  $M_y$ , and  $M_z$ , over a  $10^5\tau$  simulation trajectory are traced in red, blue, and green, respectively, in

units of  $ea$  ( $e$  is elementary protonic charge;  $a$  is reference bond length) for the sv30,  $T_0^* = 6.0$  system in (a) and (b) as an example. As a guide for the eye,  $\mathbf{M} = \mathbf{0}$  is marked by a white (c, d, e) or black (f, g, h) horizontal line. Shown in (c)–(e) are the total dipole moments of (c) polyampholytes and of (d) dipole solvent molecules inside the droplet (c and d), and (e) the total dipole moment of the simulation box as a whole, all for the entire duration of the simulated trajectory. (f)–(h) The last  $500\tau$  of the  $\mathbf{M}$  variations in (c)–(e), respectively, are depicted using in a zoomed-in horizontal scale for time = 99,  $500\tau$  to 100,  $000\tau$ .

Taking a first step to address this interesting question, we compute, using our molecular dynamics model, the overall effective relative permittivities of droplets that account for contributions from the polar solvent as well as the polyampholytes themselves (Fig. 14). In the context of biomolecular modeling, this overall effective  $\epsilon_r$  would approximate the relative permittivity experienced by client molecules (test charges) inside a biomolecular condensate. Fig. 14a shows that this overall droplet  $\epsilon_r$  increases dramatically with  $-SCD$  of the sequences. For the three sequences considered, the overall droplet  $\epsilon_r$ s estimated from largely equilibrated trajectories barring one exception (Fig. 14b) far exceed the model solvent’s effective  $\epsilon_r$  of 4.0. For sv30, the overall droplet  $\epsilon_r$ s at low temperatures likely exceed even the  $\approx 80$  value for bulk water, although the simulation at  $T_0^* = 3.0$  for this sequence has not fully equilibrated (top black curve in Fig. 14b). These high values of overall droplet  $\epsilon_r$  is likely caused by the highly charged nature of the model polyampholytes we studied. Intuitively, one may expect less dramatic dielectric effects in biomolecular condensates scaffolded by natural IDP polyampholytes that are less charged. By comparison,  $\epsilon_r$  of folded proteins has been estimated by experiment on dry protein powder<sup>129</sup> and an early theoretical treatment<sup>65</sup> to be  $\approx 2$ –4, whereas subsequent experiments on dry synthetic polypeptides<sup>130</sup> suggest higher values of up to 20 and experimental  $pK_a$  measurements of buried charged residues indicate  $\epsilon_r \approx 10$ –12 in the largely nonpolar core of a folded protein.<sup>66,67</sup> Simulations using explicit atomic models of water<sup>68,71</sup> affording  $\epsilon_r \approx 15$ –40 for natural folded proteins are roughly in line with the more recent experiments though the simulated  $\epsilon_r$  value for some folded protein can be as high as  $\approx 58$  (ref. 71). Whether condensates of dynamic, highly charged natural IDPs can result in significantly higher  $\epsilon_r$  values and related questions regarding the spatial heterogeneity of the dielectric environment within condensed droplets remain to be further explored.

As an illustration of the relationship between dielectric properties and the dynamics of a condensed polyampholyte-rich droplet, fluctuations of various components of dipole moment,  $\mathbf{M}$ , in the sv30,  $T_0^* = 6.0$  system are provided in Figs. 14c–h. We note that the  $\mathbf{M}$  fluctuation of the dipole solvent is essentially isotropic as expected (nearly identical amplitudes in the  $x$ ,  $y$ , and  $z$  directions in Fig. 14d), whereas the  $\mathbf{M}$  fluctuation of the polyampholytes is significantly smaller in amplitude in the  $z$  direction than in the  $x$  and  $y$  directions (green curve has narrower range than the red and blue curves in Fig. 14c). This

is because in our simulation system, the droplet has two polyampholyte-solvent interfaces along the  $z$  directions but no such interfaces along the  $x, y$  directions because of periodic boundary conditions (Fig. 5), hence for the finite-size (small) droplet in the present model, fluctuation in the  $z$  direction is relatively much more constrained.

The zoomed-in curves in Figs. 14f–h focusing on the large-time equilibrated regime indicate that the  $\mathbf{M}$  fluctuations of dipole solvent molecules (Fig. 14g) and polyampholytes (Fig. 14f) involve very different time scales, exhibiting much slower  $\mathbf{M}$  variation with respect to the Langevin molecular dynamics time (horizontal variable in Fig. 14c–h, denoted as  $t_{\text{MD}}$  below) for the polyampholytes than for the dipole solvent. We quantify this difference by calculating the temporal correlation  $\langle \mathbf{M}(t_{\text{MD}} + t_{\text{MD},0}) \cdot \mathbf{M}(t_{\text{MD},0}) \rangle_{t_{\text{MD},0}} / \langle \mathbf{M}(t_{\text{MD},0}) \cdot \mathbf{M}(t_{\text{MD},0}) \rangle_{t_{\text{MD},0}} \approx \exp(-t_{\text{MD}}/\tau_{\mathbf{M}})$  from the simulated trajectory, finding that the relaxation time  $\tau_{\mathbf{M}} \approx 141.0\tau$  for the polyampholytes is  $\sim 350$  times that of the  $\tau_{\mathbf{M}} \approx 0.406\tau$  for the dipole solvent. This result suggests, perhaps not too surprisingly, that the polyampholyte chain molecules and the small dipole solvent molecules have very different dielectric response times. Whereas investigations of dielectric dispersion of aqueous protein systems have primarily concerned with the dispersive effects of protein-water interactions,<sup>131</sup> the present results suggest that dielectric dispersion caused by chain dynamics is an aspect of the material properties of biomolecular condensates<sup>132</sup> that deserves attention as well because of its biophysical, biochemical, and potentially novel functional implications.

## CONCLUSION

In summary, our explicit-chain molecular dynamics as well as analytical theory suggest that the heterogeneous solvent dielectric environment entailed by polyampholyte LLPS—with less solvent inside the condensed phase than outside—entails in most cases a minor but nonetheless appreciable enhancement of LLPS propensity relative to that predicted by polyampholytes interacting in a uniform dielectric environment carrying the bulk-solvent relative permittivity. While these observations are based on simplified models, they suggest that the common approach of modeling polyampholyte LLPS with a uniform  $\epsilon \approx 80$  likely leads to a minor underestimation of LLPS propensity. The extent of the expected small error, however, has to be ascertained by further investigation, using simulations with realistic water models if possible. Further advances building on the analytical formulation developed here should also provide a complementary approach to address this basic question. Although concentration-dependent solvent permittivity likely incurs only a minor effect on the stability of polyampholyte condensates, we find that the overall dielectric environment contributed by both the polar solvent and the polyampholyte scaffold inside a condensate can be highly sensitive to the sequence charge pattern of the polyampholyte, likely resulting in

a complex combination of dielectric responses characterized by vastly different time scales. All told, much about the complexity of the internal dielectric environment of biomolecular condensates and its biophysical and biochemical ramifications remain to be investigated.

**Acknowledgements.** We thank Julie Forman-Kay for helpful discussions. Financial support for this work was provided by Canadian Institutes of Health Research grant NJT-155930 and Natural Sciences and Engineering Research Council of Canada Discovery grant RGPIN-2018-04351. We are grateful for the computational resources provided by Compute/Calcul Canada.

The authors declare no conflict of interest.

## References

---

- <sup>1</sup> Banani, S. F.; Lee, H. O.; Hyman, A. A.; Rosen, M. K. Biomolecular condensates: organizers of cellular biochemistry. *Nat. Rev. Mol. Cell Biol.* **2017**, *18*, 285–298.
- <sup>2</sup> Hyman, A. A.; Weber, C. A.; Jülicher, F. Liquid-liquid phase separation in biology. *Annu. Rev. Cell Dev. Biol.* **2014**, *30*, 39–58.
- <sup>3</sup> Brangwynne, C. P.; Tompa, P.; Pappu, R. V. Polymer physics of intracellular phase transitions. *Nat. Phys.* **2015**, *11*, 899–904.
- <sup>4</sup> Lin, Y.-H.; Forman-Kay, J. D.; Chan, H. S. Sequence-specific polyampholyte phase separation in membraneless organelles. *Phys. Rev. Lett.*, 2016, **117**, 178101.
- <sup>5</sup> Alberti, S.; Gladfelter, A.; Mittag, T. Considerations and challenges in studying liquid-liquid phase separation and biomolecular condensates. *Cell* **2019**, *176*, 419–434.
- <sup>6</sup> Brangwynne, C. P.; Eckmann, C. R.; Courson, D. S.; Rybarska, A.; Hoege, C.; Gharakhani, J.; Jülicher, F.; Hyman, A. A. Germline P granules are liquid droplets that localize by controlled dissolution/condensation. *Science* **2009**, *324*, 1729–1732.
- <sup>7</sup> Li, P.; Banjade, S.; Cheng, H. C.; Kim, S.; Chen, B.; Guo, L.; Llaguno, M.; Hollingsworth, J. V.; King, D. S.; Banani, S. F.; Russ, P. S.; Jiang, Q.-X.; Nixon, B. T.; Rosen, M. K. Phase transitions in the assembly of multivalent signalling proteins. *Nature* **2012**, *483*, 336–340.
- <sup>8</sup> Kato, M.; Han, T. W.; Xie, S.; Shi, K.; Du, X.; Wu, L. C.; Mirzaei, H.; Goldsmith, E. J.; Longgood, J.; Pei, J.; Grishin, N. V.; Frantz, D. E.; Schneider, J. W.; Chen, S.; Li, L.; Sawaya, M. R.; Eisenberg, D.; Tycko, R.; McKnight, S. I. Cell-free formation of RNA granules: low complexity sequence domains form dynamic fibers within hydrogels. *Cell* **2012**, *149*, 753–767.
- <sup>9</sup> Nott, T. J.; Petsalaki, E.; Farber, P.; Jarvis, D.; Fussner, E.; Plochowitz, A.; Craggs, T. D.; Bazett-Jones, D. P.; Pawson, T.; Forman-Kay, J. D.; Baldwin, A. J. Phase transition of a disordered nuage protein generates environmentally responsive membraneless organelles. *Mol. Cell* **2015**, *57*, 936–947.
- <sup>10</sup> Molliex, A.; Temirov, J.; Lee, J.; Coughlin, M.; Kanagaraj, A. P.; Kim, H. J.; Mittag, T.; Taylor, J. P. Phase separation by low complexity domains promotes stress granule assembly and drives pathological fibrillization. *Cell* **2015**, *163*, 123–133.
- <sup>11</sup> Lin, Y.; Protter, D. S. W.; Rosen, M. K.; Parker, R. Formation and maturation of phase-separated liquid droplets by RNA-binding proteins. *Mol. Cell* **2015**, *60*, 208–219.
- <sup>12</sup> Bergeron-Sandoval, L.P.; Safaee, N.; Michnick, S. W. Mechanisms and consequences of macromolecular phase separation. *Cell* **2016**, *165*, 1067–1079.

- <sup>13</sup> Shin, Y.; Brangwynne, C.P. Liquid phase condensation in cell physiology and disease. *Science* **2017**, *357*, eaaf4382.
- <sup>14</sup> Boeynaems, S.; Alberti, S.; Fawzi, N. L.; Mittag, T.; Polymenidou, M.; Rousseau, F.; Schymkowitz, J.; Shorter, J.; Wolozin, B.; Van Den Bosch, L.; Tompa, P.; Fuxreiter, M. Protein phase separation: a new phase in cell biology. *Trends Cell Biol.* **2018**, *28*, 420–435.
- <sup>15</sup> Ladouceur, A.-M.; Parmar, B. S.; Biedzinski, S.; Wall, J.; Tope, S. G.; Cohn, D.; Kim, A.; Soubry, N.; Reyes-Lamothe, R.; Weber, S. C. Clusters of bacterial RNA polymerase are biomolecular condensates that assemble through liquid–liquid phase separation. *Proc. Natl. Acad. Sci. U.S.A.* **2020**, *117*, 18540–18549.
- <sup>16</sup> Chong, P. A.; Forman-Kay, J. D. Liquid-liquid phase separation in cellular signaling systems. *Curr. Opin. Struct. Biol.* **2016**, *41*, 180–186.
- <sup>17</sup> Li, X.-H.; Chavali, P. L.; Pancsa, R.; Chavali, S.; Babu, M. M. Function and regulation of phase-separated biological condensates. *Biochemistry* **2018**, *57*, 2452–2461.
- <sup>18</sup> Chen, X.; Wu, X.; Wu, H.; Zhang, M. Phase separation at the synapse. *Nat. Neurosci.* **2020**, *23*, 301–310.
- <sup>19</sup> Cinar, H.; Oliva, R.; Lin, Y.-H.; Chen, X.; Zhang, M.; Chan, H. S.; Winter, R. Pressure sensitivity of SynGAP/PSD-95 condensates as a model for postsynaptic densities and its biophysical and neurological ramifications. *Chem. Eur. J.* **2020**, *26*, 11024–11031.
- <sup>20</sup> Gomes, E., and Shorter, J. The molecular language of membraneless organelles. *J. Biol. Chem.* **2019**, *294*, 7115–7127.
- <sup>21</sup> Laflamme, G.; Mekhail, K. Biomolecular condensates as arbiters of biochemical reactions inside the nucleus. *Commun. Biol.* **2020**, *3*, 773.
- <sup>22</sup> Schaffert, N.; Hossbach, M.; Heintzmann, R.; Achsel, T.; Lührmann, R. RNAi knockdown of hPrp31 leads to an accumulation of U4/U6 di-snRNPs in Cajal bodies. *EMBO J.* **2004**, *23*, 3000–3009.
- <sup>23</sup> Nott, T. J.; Craggs, T. D.; Baldwin, A. J. Membraneless organelles can melt nucleic acid duplexes and act as biomolecular filters. *Nat. Chem.* **2016**, *8*, 569–575.
- <sup>24</sup> Lu, Y.; Wu, T.; Gutman, O.; Lu, H.; Zhou, Q.; Henis, Y. I.; Luo, K. Phase separation of TAZ compartmentalizes the transcription machinery to promote gene expression. *Nat. Cell Biol.* **2020**, *22*, 453–464.
- <sup>25</sup> Csizmok, V.; Follis, A. V.; Kriwacki, R. W.; Forman-Kay, J. D. Dynamic protein interaction networks and new structural paradigms in signaling. *Chem. Rev.* **2016**, *116*, 6424–6462.
- <sup>26</sup> Monahan, Z.; Ryan, V. H.; Janke, A. M.; Burke, K. A.; Rhoads, S. N.; Zerze, G. H.; O’Meally, R.; Dignon, G. L.; Conicella, A. E.; Zheng, W.; Best, R. B.; Cole, R. N.; Mittal, J.; Shewmaker, F.; Fawzi N. L. Phosphorylation of the FUS low-complexity domain disrupts phase separation, aggregation, and toxicity. *EMBO J.* **2017**, *36*, 2951–2967.
- <sup>27</sup> Elbaum-Garfinkle, S.; Kim, Y.; Szczepaniak, K.; Chen, C. C.-H.; Eckmann, C. R.; Myong,

- S.; Brangwynne, C. P. The disordered P granule protein LAF-1 drives phase separation into droplets with tunable viscosity and dynamics. *Proc. Natl. Acad. Sci. U.S.A.* **2015**, *112*, 7189–7194.
- <sup>28</sup> van der Lee, B.; Buljan, M.; Lang, B.; Weatheritt, R. J.; Daughdrill, G. W.; Dunker, A. K.; Fuxreiter, M.; Gough, J.; Gsponer, J.; Jones, D. T.; Kim, P. M.; Kriwacki, R. W.; Oldfield, C. J.; Pappu, R. V.; Tompa, P.; Uversky, V. N.; Wright, P. E.; Babu, M. M. Classification of intrinsically disordered regions and proteins. *Chem. Rev.* **2014**, *114*, 6589–6631.
- <sup>29</sup> Lin, Y.-H.; Song, J.; Forman-Kay, J. D.; Chan, H. S. Random-phase-approximation theory for sequence-dependent, biologically functional liquid-liquid phase separation of intrinsically disordered proteins. *J. Mol. Liq.*, 2017, **228**, 176–193.
- <sup>30</sup> Zhou, H.-X.; Pang, X. Electrostatic interactions in protein structure, folding, binding, and condensation. *Chem. Rev.* **2018**, *118*, 1691–1741.
- <sup>31</sup> Vernon, R. M.; Chong, P. A.; Tsang, B.; Kim, T. H.; Bah, A.; Farber, P.; Lin, H.; Forman-Kay, J. D. Pi-Pi contacts are an overlooked protein feature relevant to phase separation. *eLife* **2018**, *7*, e31486.
- <sup>32</sup> Wang, J.; Choi, J. M.; Holehouse, A. S.; Lee, H. O.; Zhang, X.; Jahnel, M.; Maharana, S.; Lemaitre, R.; Pozniakovsky, A.; Drechsel, D.; Poser, I.; Pappu, R. V.; Alberti, S.; Hyman, A. A. A molecular grammar governing the driving forces for phase separation of prion-like RNA binding proteins. *Cell* **2018**, *174*, 688–699.
- <sup>33</sup> Vernon, R. M.; Forman-Kay, J. D. First-generation predictors of biological protein phase separation. *Curr. Opin. Struct. Biol.* **2019**, *58*, 88–96.
- <sup>34</sup> Martin, E. W.; Holehouse, A. S.; Peran, I.; Farag, M.; Incicco, J. J.; Bremer, A.; Grace, C. R.; Soranno, A.; Pappu, R. V.; Mittag, T. Valence and patterning of aromatic residues determine the phase behavior of prion-like domains. *Science* **2020**, *367*, 694–699.
- <sup>35</sup> Das, S.; Lin, Y.-H.; Vernon, R. M.; Forman-Kay, J. D.; Chan, H. S. Comparative roles of charge,  $\pi$ , and hydrophobic interactions in sequence-dependent phase separation of intrinsically disordered proteins. *Proc. Natl. Acad. Sci. U.S.A.* **2020**, *117*, 28795–28805.
- <sup>36</sup> Muiznieks, L. D.; Sharpe, S.; Pomès, R.; Keeley, F. W. Role of liquid–liquid phase separation in assembly of elastin and other extracellular matrix proteins. *J. Mol. Biol.* **2018**, *430*, 4741–4753.
- <sup>37</sup> Lin, Y.-H.; Forman-Kay, J. D.; Chan, H. S. Theories for sequence-dependent phase behaviors of biomolecular condensates. *Biochemistry* **2018**, *57*, 2499–2508.
- <sup>38</sup> Cinar, H.; Cinar, S.; Chan, H. S.; Winter, R. Pressure-induced dissolution and reentrant formation of condensed, liquid-liquid phase-separated elastomeric  $\alpha$ -elastin. *Chem. Eur. J.* **2018** *24*, 8286–8291.
- <sup>39</sup> Dignon, G. L.; Zheng, W.; Kim, Y. C.; Mittal, J. Temperature-controlled liquid-liquid phase separation of disordered proteins. *ACS Cent. Sci.* **2019**, *5*, 821–830.

- <sup>40</sup> Cinar, H.; Fetahaj, Z.; Cinar, S.; Vernon, R. M.; Chan, H. S.; Winter, R. Temperature, hydrostatic pressure, and osmolyte effects on liquid-liquid phase separation in protein condensates: Physical chemistry and biological implications. *Chem. Eur. J.* **2019**, *57*, 13049–13069.
- <sup>41</sup> Bianchi, G.; Longhi, S.; Grandori, R.; Brocca, S. Relevance of electrostatic charges in compactness, aggregation, and phase separation of intrinsically disordered proteins. *Int. J. Mol. Sci.* **2020**, *21*, 6208.
- <sup>42</sup> Yeong, V.; Werth, E. G.; Brown, L. M.; Obermeyer, A. C. Formation of biomolecular condensates in bacteria by tuning protein electrostatics. *ACS Cent. Sci.* **2020**, *6*, 2301–2310.
- <sup>43</sup> Tsang, B.; Arsenaault, J.; Vernon, R. M.; Lin, H.; Sonenberg, N.; Wang, L. Y.; Bah, A.; Forman-Kay, J. D. Phosphoregulated FMRP phase separation models activity-dependent translation through bidirectional control of mRNA granule formation. *Proc. Natl. Acad. Sci. U.S.A.* **2019**, *116*, 4218–4227.
- <sup>44</sup> Schuster, B. S.; Dignon, G. L.; Tang, W. S.; Kelley, F. M.; Ranganath, A. K.; Jahnke, C. N.; Simplins, A. G.; Regy, R. M.; Hammer, D. A.; Good, M. C.; Mittal, J. Identifying sequence perturbations to an intrinsically disordered protein that determine its phase separation behavior. *Proc. Natl. Acad. Sci. U.S.A.* **2020**, *117*, 11421–11431.
- <sup>45</sup> Das, R. K.; Pappu, R. V. Conformations of intrinsically disordered proteins are influenced by linear sequence distributions of oppositely charged residues. *Proc. Natl. Acad. Sci. U.S.A.* **2013**, *110*, 13392–13397.
- <sup>46</sup> Sawle, L.; Ghosh, K. A theoretical method to compute sequence dependent configurational properties in charged polymers and proteins. *J. Chem. Phys.* **2015**, *143*, 085101.
- <sup>47</sup> Zhao, M.; Zhou, J.; Su, C.; Niu, L.; Liang, D.; Li, B. Complexation behavior of oppositely charged polyelectrolytes: Effect of charge distribution. *J. Chem. Phys.* **2015**, *142*, 204902.
- <sup>48</sup> Lin, Y.-H.; Chan, H. S. Phase separation and single-chain compactness of charged disordered proteins are strongly correlated. *Biophys. J.* **2017**, *112*, 2043–2046.
- <sup>49</sup> Brady, J. P.; Farber, P. J.; Sekhar, A.; Lin, Y.-H.; Huang, R.; Bah, A.; Nott, T. J.; Chan, H. S.; Baldwin, A. J.; Forman-Kay, J. D.; Kay, L. E. Structural and hydrodynamic properties of an intrinsically disordered region of a germ cell-specific protein on phase separation. *Proc. Natl. Acad. Sci. U.S.A.* **2017**, *114*, E8194–E8203.
- <sup>50</sup> Amin, A. N.; Lin, Y.-H.; Das, S.; Chan, H. S. Analytical theory for sequence-specific binary fuzzy complexes of charged intrinsically disordered proteins. *J. Phys. Chem. B* **2020**, *124*, 6709–6720.
- <sup>51</sup> Lin, Y. -H.; Brady, J. P.; Forman-Kay J. D.; Chan, H. S. Charge pattern matching as a ‘fuzzy’ mode of molecular recognition for the functional phase separations of intrinsically disordered proteins. *New J. Phys.* **2017**, *19*, 115003.
- <sup>52</sup> Chang, L.-W.; Lytle, T. K.; Radhakrishna, M.; Madinya, J. J.; Vélez, J.; Sing, C. E.; Perry, S. L. Sequence and entropy-based control of complex coacervates. *Nat. Comm.* **2017**, *8*, 1273.

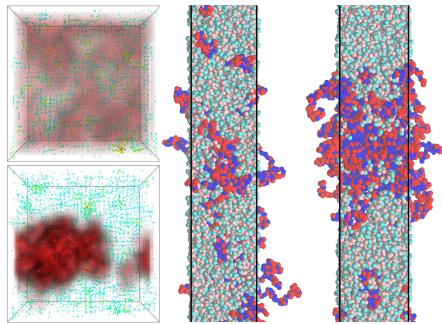
- <sup>53</sup> Lin, Y.-H.; Brady, J. P.; Chan, H. S.; Ghosh, K. A unified analytical theory of heteropolymers for sequence-specific phase behaviors of polyelectrolytes and polyampholytes. *J. Chem. Phys.* **2020**, *152*, 045102.
- <sup>54</sup> Dignon, G. L.; Zheng, W.; Kim, Y. C.; Best, R. B.; Mittal, J. Sequence determinants of protein phase behavior from a coarse-grained model. *PLoS Comput. Biol.* **2018**, *14*, e1005941.
- <sup>55</sup> Das, S.; Eisen, A.; Lin, Y.-H.; Chan, H. S. A lattice model of charge-pattern-dependent polyampholyte phase separation. *J. Phys. Chem. B* **2018**, *122*, 5418–5431.
- <sup>56</sup> Dignon, G. L.; Zheng, W.; Best, R. B.; Kim, Y. C.; Mittal, J. Relation between single-molecule properties and phase behavior of intrinsically disordered proteins. *Proc. Natl. Acad. Sci. U.S.A.* **2018**, *115*, 9929–9934.
- <sup>57</sup> Das, S.; Amin, A. N.; Lin, Y.-H.; Chan, H. S. Coarse-grained residue-based models of disordered protein condensates: Utility and limitations of simple charge pattern parameters. *Phys. Chem. Chem. Phys.* **2018**, *20*, 28558–28574.
- <sup>58</sup> Hazra, M. K.; Levy, Y. Charge pattern affects the structure and dynamics of polyampholyte condensates. *Phys. Chem. Chem. Phys.* **2020**, *22*, 19368–19375.
- <sup>59</sup> Robichaud, N. A. S.; Saika-Voivod, I.; Wallin, S. Phase behavior of blocky charge lattice polymers: Crystals, liquids, sheets, filaments, and clusters. *Phys. Rev. E* **2019**, *100*, 052404.
- <sup>60</sup> Lin, Y.; McCarty, J.; Rauch, J. N.; Delaney, K. T.; Kosik, K. S.; Fredrickson, G. H.; Shea, J.-E.; Han, S. Narrow equilibrium window for complex coacervation of tau and RNA under cellular conditions *eLife* **2019**, *8*, e42571.
- <sup>61</sup> McCarty, J.; Delaney, K. T.; Danielsen, S. P. O.; Fredrickson, G. H.; Shea, J.-E. Complete phase diagram for liquid-liquid phase separation of intrinsically disordered proteins. *J. Phys. Chem. Lett.* **2019**, *10*, 1644–1652.
- <sup>62</sup> Danielsen, S. P. O.; McCarty, J.; Shea, J.-E.; Delaney, K. T.; Fredrickson, G. H. Molecular design of self-coacervation phenomena in block polyampholytes. *Proc. Natl. Acad. Sci. U.S.A.* **2019**, *116*, 8224–8232.
- <sup>63</sup> Danielsen, S. P. O.; McCarty, J.; Shea, J.-E.; Delaney, K. T.; Fredrickson, G. H. Small ion effects on self-coacervation phenomena in block polyampholytes. *J. Chem. Phys.* **2019**, *151*, 034904.
- <sup>64</sup> Pal, T.; Wessén, J.; Das, S.; Chan, H. S. Subcompartmentalization of polyampholyte species in organelle-like condensates is promoted by charge-pattern mismatch and strong excluded-volume interaction. *Phys. Rev. E* **2021**, in press (accepted for publication); preprint available on arXiv: <https://arxiv.org/abs/2006.12776>.
- <sup>65</sup> Gilson, M. K.; Honig, B. H. The dielectric constant of a folded protein. *Biopolymers* **1986**, *25*, 2097–2119.
- <sup>66</sup> García-Moreno, B.; Dwyer, J.; Gittis, A. G.; Lattman, E. E.; Spencer, D. S.; Stites, W. E. Experimental measurement of the effective dielectric in the hydrophobic core of a protein.

- Biophys. Chem.* **1997**, *64*, 211–224.
- <sup>67</sup> Dwyer, J. J.; Gittis, A. G.; Karp, D. A.; Lattman, E. E.; Spencer, D. S.; Stites, W. E.; García-Moreno E, B. High apparent dielectric constants in the interior of a protein reflect water penetration. *Biophys. J.* **2000**, *79*, 1610–1620.
- <sup>68</sup> Pitera, J. W.; Faltá, M.; van Gunsteren, W. F. Dielectric properties of proteins from simulation: The effects of solvent, ligands, pH, and temperature. *Biophys. J.* **2001**, *80*, 2546–2555.
- <sup>69</sup> Schutz, C. N.; Warshel, A. What are the dielectric “constants” of proteins and how to validate electrostatic models? *Proteins* **2001**, *44*, 400–417.
- <sup>70</sup> Guest, W. C.; Cashman, N. R.; Plotkin, S. S. A theory for the anisotropic and inhomogeneous dielectric properties of proteins. *Phys. Chem. Chem. Phys.* **2011**, *13*, 6286–6295.
- <sup>71</sup> Sawle, L.; Huihui, J.; Ghosh, K. All-atom simulations reveal protein charge decoration in the folded and unfolded ensemble is key in thermophilic adaptation. *J. Chem. Theory Comput.* **2017**, *13*, 5065–5075.
- <sup>72</sup> Cuervo, A.; Dans, P. D.; Carrascosa, J. L.; Orozco, M.; Gomila, G.; Fumagalli, L. Direct measurement of the dielectric polarization properties of DNA. *Proc. Natl. Acad. Sci. U.S.A.* **2014**, *111*, E3624–E3630.
- <sup>73</sup> Fumagalli, L.; Esfandiar, A.; Fabregas, R.; Hu1, S.; Ares, P.; Janardanan, A.; Yang, Q.; Radha1, B.; Taniguchi, T.; Watanabe, K. Gomila, G.; Novoselov, K. S.; Geim, A. K. Anomalous low dielectric constant of confined water. *Science* **2018**, *360*, 1339–1342.
- <sup>74</sup> Bragg, W. L.; Pippard, A. B. The form birefringence of macromolecules. *Acta Cryst.* **1953**, *6*, 865–867.
- <sup>75</sup> Jackson, J. D. *Classical Electrodynamics* (2nd edition); Wiley, :New York, 1975; pp 154–155.
- <sup>76</sup> Markel, V. A. Introduction to the Maxwell Garnett approximation: Tutorial. *J. Opt. Soc. Am. A* **2016** *33* 1244–1256.
- <sup>77</sup> Ferreira, L. A.; Loureiro, J. A.; Gomes, J.; Uversky, V. N.; Madeira, P. P.; Zaslavsky, B. Y. Why physicochemical properties of aqueous solutions of various compounds are linearly interrelated. *J. Mol. Liq.* **2016**, *221*, 116–123.
- <sup>78</sup> Moreau, N. G.; Martin, N.; Gobbo, P.; Tang, T.-Y. D.; Mann, S. Spontaneous membrane-less multi-compartmentalization via aqueous two-phase separation in complex coacervate microdroplets. *Chem. Commun.* **2020**, *56*, 12717.
- <sup>79</sup> Yildirim, A.; Sharma, M.; Varner, B. M.; Fang, L.; Feig, M. Conformational preferences of DNA in reduced dielectric environments. *J. Phys. Chem. B* **2014**, *118*, 10874–10881.
- <sup>80</sup> Arscott, P. G.; Ma, C.; Wenner, J. R.; Bloomfield, V. A. DNA condensation by cobalt hexaamine(III) in alcohol-water mixtures: Dielectric constant and other solvent effects. *Biopolymers*, **1995**, *36*, 345–364.
- <sup>81</sup> Nakashima, K. K.; Vibhute, M. A.; Spruijt, E. Biomolecular chemistry in liquid phase separated compartments. *Frontiers Mol. Biosci.* **2019**, *6*, 21.

- <sup>82</sup> Milin, A. N.; Deniz, A. A. Reentrant phase transitions and non-equilibrium dynamics in membraneless organelles. *Biochemistry* **2018**, *57*, 2470–2477.
- <sup>83</sup> Zaslavsky, B. Y.; Uversky, V. N. In aqua veritas: The indispensable yet mostly ignored role of water in phase separation and membrane-less organelles. *Biochemistry* **2018**, *57*, 2437–2451.
- <sup>84</sup> Zaslavsky, B. Y.; Ferreira, L. A.; Darling, A. L.; Uversky, V. N. The solvent side of proteinaceous membrane-less organelles in light of aqueous two-phase systems. *Int. J. Biol. Macromol.* **2018**, *117*, 1224–1251.
- <sup>85</sup> Pliss, A.; Levchenko, S. M.; Liu, L.; Peng, X.; Ohulchanskyy, T. Y.; Roy, I.; Kuzmin, A. N.; Qu, J.; Prasad, P. N. Cycles of protein condensation and discharge in nuclear organelles studied by fluorescence lifetime imaging. *Nat. Comm.* **2019**, *10*, 455.
- <sup>86</sup> Zheng, W.; Dignon, G. L.; Jovic, N.; Xu, X.; Regy, R. M.; Fawzi, N. L.; Kim, Y. C.; Best, R. B.; Mittal, J. Molecular details of protein condensates probed by microsecond long atomistic simulations. *J. Phys. Chem. B* **2020**, *124*, 11671–11679.
- <sup>87</sup> Benayad, Z.; von Bülow, S.; Stelzl, L. S.; Hummer, G. Simulation of FUS protein condensates with an adapted coarse-grained model. *J. Chem. Theory Comput.* **2021**, *17*, 525–537.
- <sup>88</sup> de Jong, D. H.; Singh, G.; Bennett, W. F. D.; Arnarez, C.; Wassenaar, T. A.; Schäfer, L. V.; Periole, X.; Tieleman, D. P.; Marrink, S. J. Improved parameters for the Martini coarse-grained protein force field. *J. Chem. Theory Comput.* **2013**, *9*, 687–697.
- <sup>89</sup> Michalowsky, J.; Schäfer, L. V.; Holm, C.; Smiatek, J. A refined polarizable water model for the coarse-grained MARTINI force field with long-range electrostatic interactions. *J. Chem. Phys.* **2017**, *146*, 054501.
- <sup>90</sup> Köfinger, J.; Hummer, G.; Dellago, C. A one-dimensional dipole lattice model for water in narrow nanopores. *J. Chem. Phys.* **2009**, *130*, 154110.
- <sup>91</sup> Motevaselian, M. H.; Mashayak, S. Y.; Aluru, N. R. Extended coarse-grained dipole model for polar liquids: Application to bulk and confined water. *Phys. Rev. E* **2018**, *98*, 052135.
- <sup>92</sup> Levy, A.; Andelman, D.; Orland, H. Dielectric constant of ionic solutions: A field-theory approach. *Phys. Rev. Lett.* **2012**, *108*, 227801.
- <sup>93</sup> Levy, A.; Andelman, D.; Orland, H. Dipolar Poisson-Boltzmann approach to ionic solutions: A mean field and loop expansion analysis. *J. Chem. Phys.* **2013**, *139*, 164909.
- <sup>94</sup> Zhuang, B.; Wang, Z.-G. Statistical field theory for polar fluids. *J. Chem. Phys.* **2018**, *149*,
- <sup>95</sup> Martin, J. M.; Li, W.; Delaney, K. T.; Fredrickson, G. H. Statistical field theory description of inhomogeneous polarizable soft matter. *J. Chem. Phys.* **2016**, *145*, 154104.
- <sup>96</sup> Grzetic, D. J.; Delaney, K. T.; Fredrickson, G. H. Constrasting dielectric properties of electrolyte solutions with polar and polarizable solvents. *Phys. Rev. Lett.* **2019**, *122*, 128007.
- <sup>97</sup> Martin, J. M.; Delaney, J. T.; Fredrickson, G. H. Effect of an electric field on the stability of binary dielectric fluid mixtures. *J. Chem. Phys.* **2020**, *152*, 234901.
- <sup>98</sup> Silmore, K. S.; Howard, M. P.; Panagiotopoulos, A. Z. Vapor-liquid equilibrium and surface

- tension of fully flexible Lennard-Jones chains. *Mol. Phys.* **2017**, *115*, 320–327.
- <sup>99</sup> Mundy, C. J.; Siepmann, J. I.; Klein, M. L. Calculation of the shear viscosity of decane using a reversible multiple timestep algorithm. *J. Chem. Phys.* **1995**, *102*, 3376–3380.
- <sup>100</sup> Martin, M. G.; Siepmann, J. I. Transferable potentials for phase equilibria. 1. United-atom description of n-alkanes. *J. Phys. Chem. B* **1998**, *102*, 2569–2577.
- <sup>101</sup> Nicolas, J. P.; Smit, B. Molecular dynamics simulations of the surface tension of n-hexane, n-decane and n-hexadecane. *Mol. Phys.* **2002**, *100*, 2471–2475.
- <sup>102</sup> Pàmies, J. C.; McCabe, C.; Cummings, P. T.; Vega, L. F. Coexistence densities of methane and propane by canonical molecular dynamics and gibbs ensemble Monte Carlo simulations. *Mol. Simul.* **2003**, *29*, 463–470.
- <sup>103</sup> Weeks, J. D.; Chandler, D.; Andersen, H. C. Role of repulsive forces in determining the equilibrium structure of simple liquids. *J. Chem. Phys.* **1971**, *54*, 5237–5247.
- <sup>104</sup> Anderson, J. A.; Lorenz, C. D.; Travesset, A. General purpose molecular dynamics simulations fully implemented on graphics processing units. *J. Comput. Phys.* **2008**, *227*, 5342–5359.
- <sup>105</sup> Glaser, J.; Nguyen, T. D.; Anderson, J. A.; Lui, P.; Spiga, F.; Millan, J. A.; Morse, D. C.; Glotzer, S. C. Strong scaling of general-purpose molecular dynamics simulations on GPUs. *Comput. Phys. Comm.* **2015**, *192*, 97–107.
- <sup>106</sup> LeBard, D. N.; Levine, B. G.; Mertmann, P.; Barr, S. A.; Jusufi, A.; Sanders, S.; Klein, M. L.; Panagiotopoulos, A. Z. Self-assembly of coarse-grained ionic surfactants accelerated by graphics processing units. *Soft Matter* **2012**, *8*, 2385–2397.
- <sup>107</sup> Martínez, L.; Andrade, R.; Birgin, E. G.; Martínez, J. M. PACKMOL: A package for building initial configurations for molecular dynamics simulations. *J. Comput. Chem.* **2009**, *30*, 2157–2164.
- <sup>108</sup> Abrashkin, A.; Andelman, D.; Orland, H. Dipolar Poisson-Boltzmann equation: Ions and dipoles close to charged interfaces. *Phys. Rev. Lett.* **2007**, *99*, 077801.
- <sup>109</sup> Ballenegger, V.; Hansen, J.-P. Dielectric permittivity profiles of confined polar fluids. *J. Chem. Phys.* **2005**, *122*, 114711.
- <sup>110</sup> Stern, H. A.; Feller, S. E. Calculation of the dielectric permittivity profile for a nonuniform system: Application to a lipid bilayer simulation. *J. Chem. Phys.* **2003**, *118*, 3401–3412.
- <sup>111</sup> Zhu, H.; Yang, F.; Zhu, Y.; Li, A.; He, W.; Huang, J.; Li, G. Investigation of dielectric constants of water in a nano-confined pore. *RSC Adv.*, **2020**, *10*, 8628–8635.
- <sup>112</sup> Chan, H. S.; Dill, K. A. Solvation: How to obtain microscopic energies from partitioning and solvation experiments. *Annu. Rev. Biophys. Biomol. Struct.* **1997**, *26*, 425–459.
- <sup>113</sup> Ray, A. Solvophobic interactions and micelle formation in structure forming nonaqueous solvents. *Nature* **1971**, *231*, 313–315.
- <sup>114</sup> Malmberg, C. G.; Maryott, A. A. Dielectric constant of water from 0° to 100°C. *J. Res. Natl. Bur. Stand. (U. S.)* **1956**, *56*, 1–8.

- <sup>115</sup> Wang, Z.-G. Fluctuation in electrolyte solutions: The self energy. *Phys. Rev. E* **2010**, *81*, 021501.
- <sup>116</sup> Chandler, D. The dielectric constant and related equilibrium properties of molecular fluids: Interaction site cluster theory analysis. *J. Chem. Phys.* **1977**, *67*, 1113–1124.
- <sup>117</sup> Edwards, S. F. The statistical mechanics of polymers with excluded volume. *Proc. Phys. Soc.* **1965**, *85*, 613–624.
- <sup>118</sup> Fredrickson, G. H. *The Equilibrium Theory Of Inhomogeneous Polymers*; Oxford University Press Inc.:New York, 2006.
- <sup>119</sup> Fredrickson, G. H.; Ganesan, V.; Drolet, F. Field-theoretic computer simulation methods for polymers and complex fluids. *Macromolecules* **2002**, *35*, 16–39.
- <sup>120</sup> Parisi, G. On complex probabilities. *Phys. Lett. B* **1983**, *131*, 393–395.
- <sup>121</sup> Klauder, J. R. A Langevin approach to fermion and quantum spin correlation functions. *J. Phys. A: Math. Gen.* **1983**, *16*, L317–L319.
- <sup>122</sup> Parisi, G.; Wu, Y.-S. Perturbation theory without gauge fixing. *Scientia Sinica* **1981** *24*, 483–496.
- <sup>123</sup> Chan, H. S.; Halpern, M. B. New ghost-free infrared-soft gauges. *Phys. Rev. D* **1986**, *33*, 540–547.
- <sup>124</sup> Chan, H. S.; Halpern, M. B. Continuum-regularized quantum gravity. *Zeitschrift Für Physik C* **1987**, *36*, 669–693.
- <sup>125</sup> Lennon, E. M.; Mohler, G. O.; Ceniceros, H. D.; Garca-Cervera, C. J.; Fredrickson, G. H. Numerical solutions of the complex Langevin equations in polymer field theory. *Multiscale Modeling & Simulation* **2008**, *6*, 1347–1370.
- <sup>126</sup> Grzetic, D. J.; Delaney, K. T.; Fredrickson, G. H. The effective  $\chi$  parameter in polarizable polymeric systems: One-loop perturbation theory and field-theoretic simulations. *J. Chem. Phys.* **2018**, *148*, 204903.
- <sup>127</sup> Delaney, K. T.; Fredrickson, G. H. Theory of polyelectrolyte complexation—Complex coacervates are self-coacervates. *J. Chem. Phys.* **2017**, *146*, 224902.
- <sup>128</sup> Riggleman, R. A.; Fredrickson, G. H. Field-theoretic simulations in the gibbs ensemble. *J. Chem. Phys.* **2010**, *132*, 024104.
- <sup>129</sup> Harvey, S. C.; Hoekstra, P. Dielectric relaxation spectra of water adsorbed on lysozyme. *J. Phys. Chem.* **1972**, *76*, 2987–2994.
- <sup>130</sup> Tredgold, R. H.; Hole, P. N. Dielectric behaviour of dry synthetic polypeptides. *Biochim. Biophys. Acta* **1976**, *443*, 137–142.
- <sup>131</sup> Bone, S.; Pethig, R. Dielectric studies of the binding of water to lysozyme. *J. Mol. Biol.* **1982**, *157*, 571–575.
- <sup>132</sup> Alshareedah, I.; Kaur, T.; Banerjee, P. R. Methods for characterizing the material properties of biomolecular condensates. *Methods Enzymol.* **2021**, *646*, 143–183.



TOC graphics